JMEPEG (2015) 24:3989–4009
DOI: 10.1007/s11665-015-1651-6

1059-9495/$19.00

Effects of Ce on Inclusions, Microstructure, Mechanical Properties, and Corrosion Behavior of AISI 202 Stainless Steel

Guojun Cai and Changsheng Li

(Submitted January 28, 2015; in revised form May 10, 2015; published online August 21, 2015)

The sizes and morphologies of nonmetallic inclusions, microhardness, tensile strength, and Charpy impact toughness in AISI 202 stainless steel with different Ce contents were synthetically analyzed by means of SEM, TEM, microhardness tester, and tensile and Charpy impact tests. Effects of Ce addition on the corrosion behavior were investigated in 5 wt.% H_2SO_4 solution for different periods of time through measuring AC impedance. The EIS measurements indicate that the steels with Ce addition exhibit higher R_p values than those without Ce, which illustrates the relative resistance to uniform corrosion is accompanied by an increasing Ce addition. Ce addition to AISI 202 stainless steel improves its uniform corrosion resistance owing to metamorphic inclusions and the improvement of electrode potential in matrix. Upon increasing Ce addition, the indentation morphology of samples transfers from sink-in types to pile-up types, explaining good machinability of steels containing Ce. It is witnessed from the fracture mode that Ce refines the grain size of steels, significantly increasing the strength; in the meantime, its plasticity is improved, thereby solving the contradiction between the strength and the plasticity of steels. It is concluded that AISI 202 stainless steel with 0.016 wt.% Ce addition in the mass fraction has the best mechanical properties and the uniform corrosion resistance.

Keywords AISI 202 stainless steel, Ce, metamorphic inclusions, plasticity, uniform corrosion

1. Introduction

AISI 202 stainless steel is a kind of austenitic stainless steel which uses manganese and nitrogen, substituting part of the nickel (Ref 1), and widely used in consumer products; in recent years, its use has developed rapidly, even being used for stampings and structural components of the aeroengine operating in high temperature. Based on the American Iron and Steel Institute (AISI) classification, austenitic stainless steel grades are designated by numbers in the 200-series (Fe-Cr-Ni-Mn-N stainless steels) and the 300-series (Fe-Cr-Ni stainless steels) (Ref 2). In several technical branches, the 200-series stainless steels are successfully applied as a replacement for the 300-series stainless steels; however, they also have a few disadvantages, such as higher strain-hardening exponent and poor corrosion resistance (Ref 3), which leads to some limitations for practical use. Compared with the 300-series stainless steels,developing the 200-series stainless steels with relatively low cost (Ref 4) is an important challenge owing to the shortage of nickel resources in China, which has become an overall goal of Chinese stainless steel products during 2011-2020.

In contrast to AISI 304 stainless steel, AISI 202 stainless steel is developed to be an option with 17 wt.% of chromium. Manganese is added to this steel at 6 wt.% to stabilize the austenite phase instead of nickel (Ref 5), and nickel is reduced from 8 to 5 wt.%. Research shows that twice content of manganese can make up for each unit of nickel content in terms of forming austenite phase, thereby saving nickel content to reduce the cost (Ref 6). However, adding manganese is not conducive to the corrosion resistance of stainless steel because of the existence of MnS along the grain boundary (Ref 7). In contrast, AISI 316Laustenitic stainless steel has better corrosion and oxidation resistance due to higher amounts of chromium and nickel (Ref 8). However, poor anticorrosion performance has severely impeded and limited its extensive application, and hence, development of AISI 202 stainless steel, by adding Ce to improve its corrosion resistance has been proposed elsewhere (Ref 9, 10). With strong chemical activities and rather large atomic radius, Ce can react easily with many elements such as

Nomenclature

EIS	Electrochemical impedance spectroscopy
JK	Standard Swedish Jemkontoret judge picture of size of inclusions
RE	Rare earth
R_p	Polarization resistance value (Ω)
b_a	Tafel slope of anodic reaction (mV)
b_c	Tafel slope of cathodic reaction(mV)
I_{corr}	Corrosion current density (Amp/cm)
E_{corr}	Corrosion potential (Volts)
$E_{M^{n+}}$	Metal electrode potential (Volts)
E_{H_2}	Hydrogen electrode potential (Volts)
i_c^0, i_a^0	Exchange current density of anode and cathode (Amp/cm)
E_{e,H^+}	Hydrogen balance potential (Volts)
η_{H_2}	Overpotential of hydrogen evolution (Volts)

Guojun Cai and **Changsheng Li,** State Key Laboratory of Rolling and Automation, Northeastern University, Shenyang 110819, China. Contact e-mail: cgj197800@163.com.

H, O, N, S, Si, etc., and can also play a favorable role in steels (Ref 11), when employed, by protecting steels and other metallic alloys against corrosion (Ref 12).

Many studies have indicated that chromium compounds in the rust layer of Cr-containing weathering steels partly replace iron species in the corrosion products to produce a more protective rust layer. The enrichment of chromium in the rust layer acts as a barrier to corrosion (Ref 13). In 5 wt.% H_2SO_4 solution, very small cathode and anode of corrosion cell are in uncertain positions (Ref 14). Hence, the whole surface is in the active state, and the energy on the surface goes up and down everywhere, which leads to the uniform corrosion (Ref 15). Trace RE can enhance the stability of the passive film, thereby improving the corrosion resistance of steel (Ref 16).

In conventional steels, the fracture toughness generally decreases as the yield strength increases. Conversely, the fracture toughness will be high when the yield strength is low. This means that a combination of high strength and high fracture toughness cannot easily be obtained in most conventional steels (Ref 17). Scholars have performed a great deal of research work to find a method through microalloying, thereby attaining high strength and fracture toughness. It was found that addition of the rare earth elements into the steel was a kind of microalloying method.

Some scholars had shown that the modification process with RE was an important method that is used to improve the structures and properties of ferrous alloys (Ref 18). Wang et al. (Ref 19) found that the segregation of rare earth elements along the grain boundary was helpful in improving the strength of a low expansion superalloy. Hao et al. (Ref 20) suggested that the rare earth elements refined the ferrite grain size in their studies on medium carbon steel. Li et al. (Ref 21) proposed the rare earth elements segregate at the grain boundary, improv

ing the mechanical properties and the oxidation resistance of Ni-16Mo-7Cr-4Fe alloy.

At present, most of the researches on the corrosion of stainless steel have focused mostly on rust layer. However, no systematic studies have yet been presented, investigating the effects of Ce addition on nonmetallic inclusions and the mechanism of uniform corrosion, especially for AISI 202 stainless steel; effects of Ce on mechanical properties and strain-hardening exponent are rarely mentioned, and the optimal Ce addition has not been studied in detail.

In the present investigation, the sizes and morphologies of nonmetallic inclusions in AISI 202 stainless steel were studied using transmission electron microscopy-energy dispersive x-ray spectroscopy (TEM-EDS), and scanning electron microscopy-energy dispersive x-ray spectroscopy (SEM-EDS), respectively. The effects of rare earth Ce on the microstructures and mechanical properties of stainless steel were evaluated using Axiovert 25 (ZEISS) microscope and transmission electron microscopy. The microhardness of AISI 202 stainless steel was tested using Japanese FM-700 microhardness tester. The influence of Ce on uniform corrosion resistance of AISI 202 stainless steel in 5 wt.% H_2SO_4 solution was studied using potentiodynamic and potentiostatic tests.

2. Experimental Procedure

2.1 Materials

In the present study, five types of AISI 202 stainless steels were manufactured in a high-frequency vacuum induction furnace. The forging temperatures of the experimental steels ranged from 1200 to 950 °C, and these ingots were forged from Φ80 mm to 25 mm × 25 mm after they were smelted. The chemical compositions of steels are presented in Table 1.

2.2 Nonmetallic Inclusions and Microstructure Studies

The nonmetallic inclusions in AISI 202 stainless steel was studied using transmission electron microscopy-energy dispersive x-ray spectroscopy (TEM-EDS), and scanning electron microscopy-energy dispersive x-ray spectroscopy (SEM-EDS). The microhardness of AISI 202 stainless steel was tested using Japanese FM-700 microhardness tester. The tensile fracture and impact fracture surfaces of the as-repaired samples were observed using scanning electron microscope (SEM).

2.3 Mechanical Properties Characterization

Tensile tests were performed at room temperature with strain rate of 5×10^{-3} s^{-1}. The transverse yield strength, ultimate tensile strength (UTS), and elongation were measured. The Charpy testing was conducted at room temperature, employing sub-size (5 mm × 10 mm × 55 mm) samples with a 2-mm-deep Charpy V-notch.

2.4 Corrosion Tests

Figure 1 presents the three-electrode test system of electrochemical experiment. Experimental steels were processed to produce horizontal standard specimens with the dimensions of 10 mm× 10 mm× 5 mm using wire-cutting machine after the heat treatment. A copper wire was welded to one of its experimental non-working surface, and they were polished before washing with anhydrous ethanol, with the samples having an exposed area of 1 cm^2 acting as the working electrodes. Electrochemical impedance spectroscopy (EIS) measurements and potentiostatic tests were performed to examine the tendency of passivation (Ref 22). The EIS measurements were made using two electrodes: the reference and counter electrodes were short-circuited and connected to a graphite bar, while the working electrode was connected to the steel (Ref 23).

Effects of Ce addition on the corrosion resistance of AISI 202 stainless steel were investigated in 5 wt.% H_2SO_4 solution; the steel samples were soaked for 1, 5, 15, 30, and 45 days,

Table 1 Compositions of experimental steel (wt.%)

Sample	C	N	Mn	P	S	Cr	Ni	Ce
A	0.071	0.115	6.014	0.0048	0.0061	17.4	5.05	0
A1	0.073	0.126	6.019	0.0046	0.0058	17.2	5.04	0.005
A2	0.071	0.118	6.015	0.0043	0.0057	17.3	5.02	0.011
A3	0.072	0.124	6.013	0.0042	0.0055	17.1	5.03	0.016
A4	0.074	0.119	6.015	0.0042	0.0054	17.2	5.04	0.022

respectively, by means of Solartron company's 1280B electrochemical station, with its potential amplitude of excitation signal being set to 10 Mv and its frequency range to 2×10^4 to 2×10^{-1} Hz. A potentiodynamic anodic polarization technique was carried out at room temperature.

3. Results and Analysis

3.1 Effects of Ce Addition on Nonmetallic Inclusions

Table 2 shows the grades of nonmetallic inclusions in the experimental steels evaluated using Zeiss optical microscope according to JK standard. With the increasing Ce content in steel, the size and quantity of nonmetallic inclusions became finer and fewer; at the same time, inclusions of coarse section gradually decreased. Compared with sample A3, there were a large number of nonmetallic inclusions in sample A4 growing together due to the high adsorption of Ce (Ref 24), which could affect properties of AISI 202 stainless steel.

Figure 2 presents the morphology of inclusions in AISI 202 stainless steel and x-ray EDS analysis. About 22-μm-long strip MnS inclusion existed in sample A without Ce which contained mostly Mn, S, Cr, and O elements, as shown in Fig. 2(a). As presented in Fig. 2(b), there were some irregular angular inclusions containing O, Al, Fe, S, Mn, and Ce elements. The analysis of energy spectrum indicated that Ce multiphase inclusion contained MnS, $CeAlO_3$, CeS, and Ce_2O_2S inclusions with a deep depression where the corrosion was formed.

As shown in Fig. 2(c), because of the high adsorption of Ce, some fine and globular inclusions (0.3 to 0.5 μm) gathered around grain boundaries to form Ce multiphase inclusion size of which was less than 2 μm, transferring the inclusions from the grain boundary to the grain inner. As shown in Fig. 2(d), some stripe inclusions disappeared, and local slight corrosions occurred around the steel matrix. The edge of inclusion in sample A4 along the grain boundary became smoother, and a deep corrosion pit occurred around the inclusion, as shown in Fig. 2(e). Some second-phase particles containing Ce with brittleness and poor corrosion resistance were distributed along grain boundaries owing to the excessive Ce content in the steel, more than its solid solubility, which was not conducive to improve its corrosion resistance.

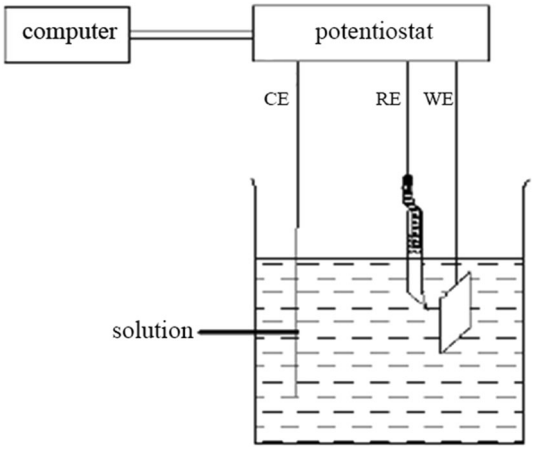

Fig. 1 Three-electrode test system

Before adding Ce to the steel, oxygen in the molten steel occurs in a dissolved state or in Al_2O_3. When Ce is added to the steel, multiphase inclusions containing $CeAlO_3$ are transferred from the grain boundary to the grain inner, making a large number of small globular inclusions gather around it, which changes the distribution of inclusions in steel, to a certain extent, purifying the steels and improving the corrosion resistance of steels.

Figure 3 presents TEM image of inclusions in AISI 202 stainless steel. A fine multiphase inclusion containing $CeAlO_3$ and Ce_2O_2S inclusions adsorbed another inclusion to form a larger multiphase inclusion (1 μm), which was consistent with the SEM observation, as shown in Fig. 3(a). Two different multiphase inclusions attracted each other and combined closely, and it is difficult to distinguish between their original interfaces, as shown in Fig. 3(b).

The nucleation process is as follows. First, owing to strong adsorption capacity, Ce atoms with strong activity can continuously spread around oxygen and sulfide inclusions of high melting point, continuing to adsorb other impurity elements in steel owing to the difference of chemistry potential. The sizes of the inclusions are associated with accumulation quantity of Ce oxide. With the increasing Ce content, more active Ce and some impurity elements cluster together. However, the aggregation of inclusions does not have a great influence on the size of inclusions (Ref 25), and they still belong to the fine-sized inclusions due to trace amounts of Ce.

Research demonstrates most of the Ce particles on the grain boundaries (Ref 26) exist in inclusions. The reaction equations are described as follows.

$$2[Ce] + Al_2O_3(S) \rightleftharpoons 2[Al] + Ce_2O_3(S), \quad \text{(Eq 1)}$$

$$[Ce] + Al_2O_3(S) \rightleftharpoons Ce_2AlO_3(S) + [Al], \quad \text{(Eq 2)}$$

$$[Ce] + MnS \rightleftharpoons CeS(S) + [Mn]. \quad \text{(Eq 3)}$$

The relevant studies indicate that Ce_2O_2S is more likely to occur with the addition of Ce. The standard formation of free energy of inclusions is calculated as follows (Ref 27).

Table 2 Grades of nonmetallic inclusions in AISI 202 stainless steel

Sample	A Level, MnS			B Level, Al_2O_3			Content of inclusions, %
	Coarse department	Thin department	Maximum size, μm	Coarse department	Thin department	Maximum size, μm	
A	3.5	0.5	19.4	3	1.5	11.6	0.827
A1	1.5	2.5	16.2	2.5	2	10.9	0.745
A2	1	4	15.3	2	2.5	9.3	0.416
A3				0.5	4.5	8.4	0.165
A4				1.5	3	9.8	0.309

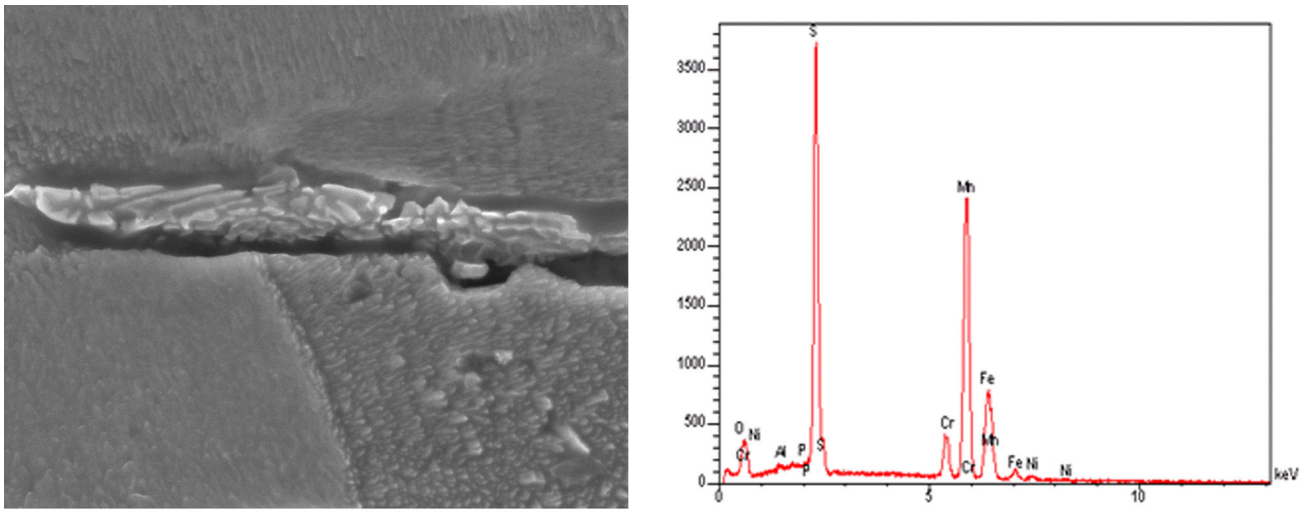

(a)

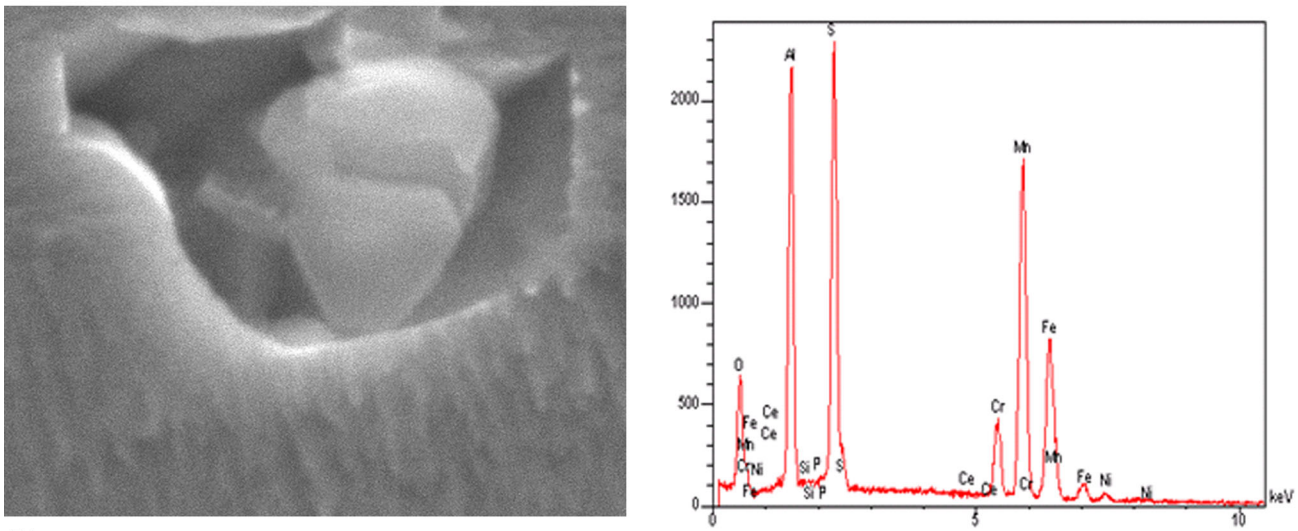

(b)

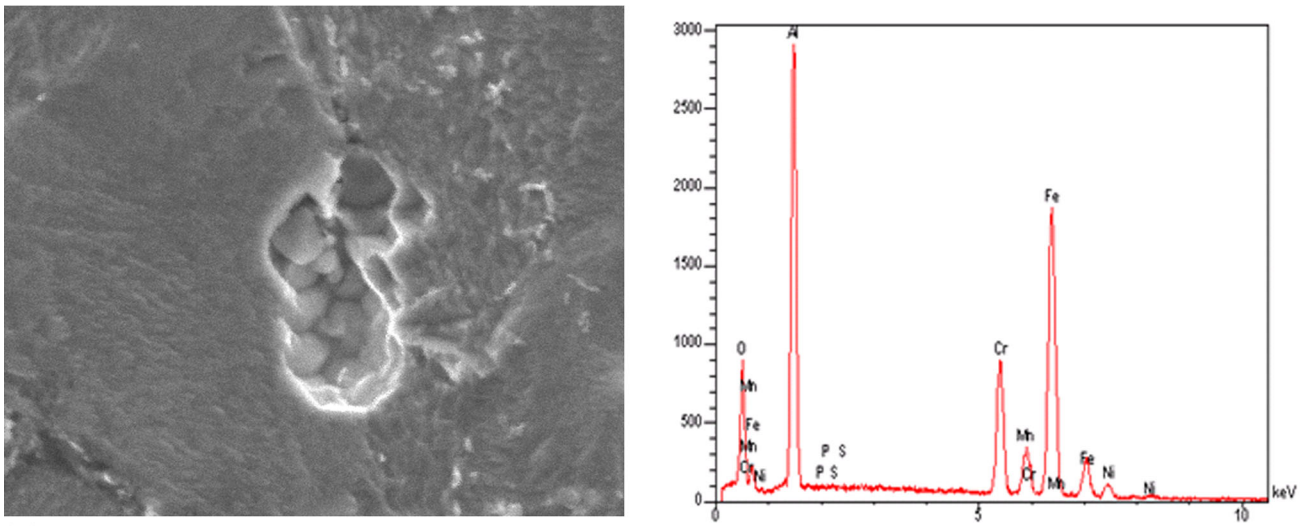

(c)

Fig. 2 Morphology of inclusions in AISI 202 stainless steel and x-ray EDS analysis: (a) Sample A without Ce addition; (b) Sample A1 with 0.005 wt.% Ce addition; (c) Sample A2 with 0.011 wt.% Ce addition; (d) Sample A3 with 0.016 wt.% Ce addition; (e) Sample A4 with 0.022 wt.% Ce addition

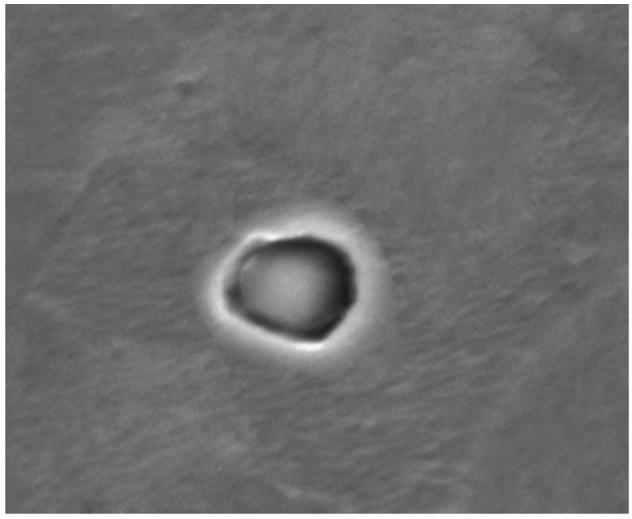

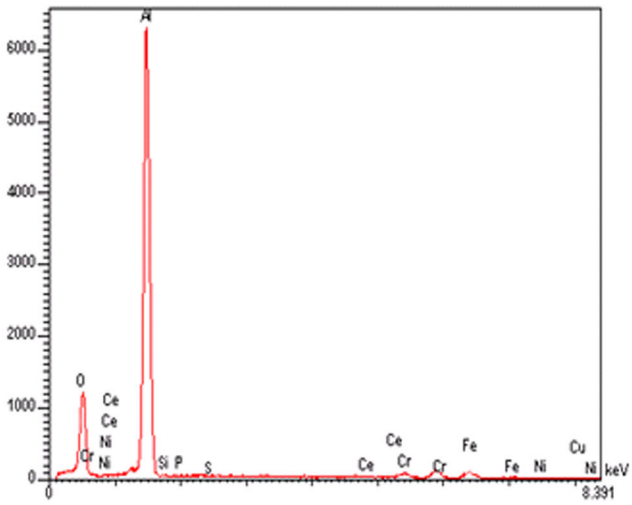

(d)

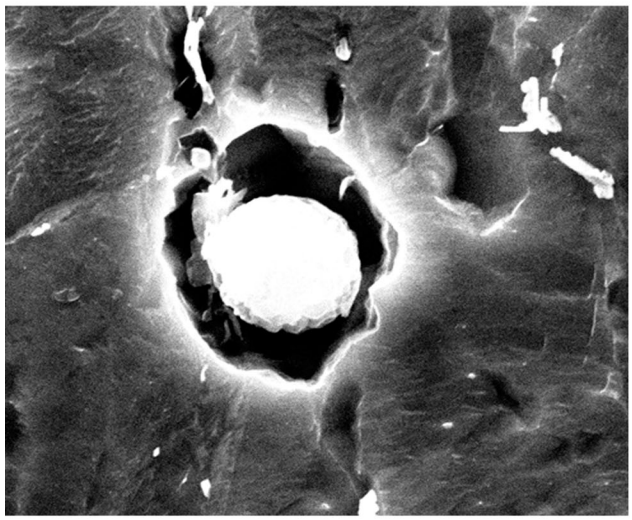

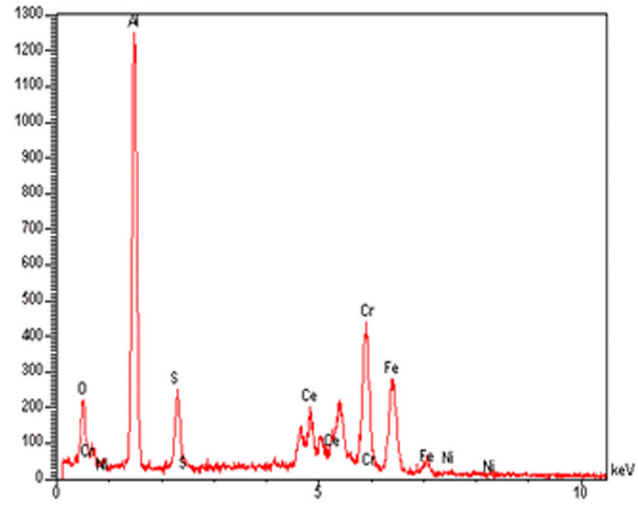

(e)

Fig. 2 continued

$$Ce_2O_3(S) \rightleftharpoons 2[Ce] + 3[O] \qquad \Delta G^0 = -714380 + 179.74T, \tag{Eq 4}$$

$$Ce_2O_2S\ (S) \rightleftharpoons 2[Ce] + 2[O] + [S] \quad \Delta G^0 = -675700 + 165.50\ T, \tag{Eq 5}$$

$$Ce_2O_3(S) + [S] \rightleftharpoons Ce_2O_2S\ (S) + [O] \quad \Delta G^0 = 38680 - 14.24T, \tag{Eq 6}$$

$$\Delta G = \Delta G^0 + RTlnJ \quad a_0 = 1.093 \times 10^{-3} \quad a_s = 4.416 \times 10^{-3} = 38680 - 14.24T + RT(a_0/a_s) = -9735J/mol < 0 \tag{Eq 7}$$

Ce_2O_3 is transformed into Ce_2O_2S according to the relevant chemical reactions.

According to the reaction's free energy and the thermodynamic conditions of Ce inclusions, Ce_2O_2S is close to the most stable inclusion. When Ce is added to the steel, the main inclusions are Ce_2O_2S, steadily controlling the morphology of sulfide.

When adding a small amount of Ce, thick and short MnS inclusions can be observed in AISI 202 stainless steel; with the Ce content increasing continuously, some finer globular CeS and Ce_2O_2S multiphase inclusions containing Ce cluster together gradually instead of MnS inclusions, thereby purifying the steel. When the Ce content is increased to more than 0.011 wt.%, long-strip MnS inclusions disappear completely.

In most cases, the distribution characteristic of inclusions is more dangerous than the total amount of inclusions in steel (Ref 28). Under the same conditions, the corrosion potential value of MnS is the minimum, and easy to corrode as the origin; by contrast, Ce_2O_2S is better than MnS in terms of the corrosion resistance, which improves the corrosion resistance

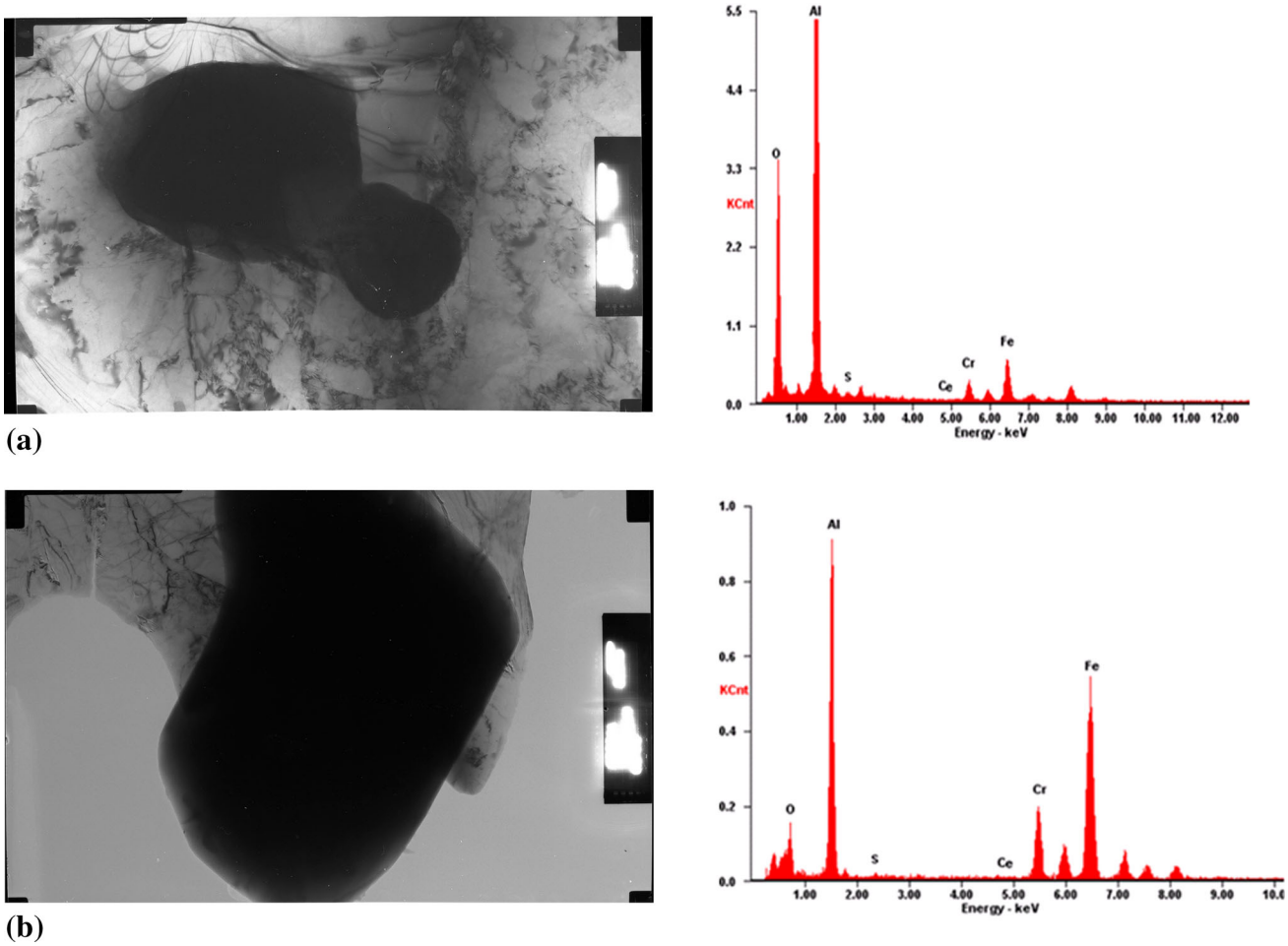

Fig. 3 TEM image of inclusions in AISI 202 stainless steel: (a) Sample A1 with 0.005 wt.% Ce addition and (b) Sample A3 with 0.016 wt.% Ce addition

of steels. The deformation energy in the grain interior is much larger than that in the grain boundary because the radius of Ce atom is about 50% larger than that of iron atom. Ce can first cluster on the grain boundary via diffusion mechanism, transfer finer metamorphic inclusions from the grain boundary into the intragranular region, decrease the damage to the steel matrix, and strengthen the grain boundary, thereby improving corrosion resistance of steels. Grain boundary is a sensitive position as pitting due to the segregation of impurity elements. Ce can purify grain boundaries and reduce impurity segregation, thereby preventing the occurrence of the corrosion.

The appropriate amount of Ce can effectively influence inclusions in many ways, such as changing their quantity, size, nature, shape, and distribution, thus improving the alloy's corrosion resistance and mechanical properties. Ce addition to the alloy can modify inclusions to attain nearly spherical shape and decrease the microcrevice between the steel matrix and the inclusion. In addition, as a cathode inclusion, multiphase inclusions containing Ce can cause metal-anode passivation, and enhance the penetrating power of corrosion medium to hinder the corrosion process.

When W ([Ce]) $\leq$ 0.011 wt.%, sulfide inclusions are controlled, and the cluster of MnS, $CeAlO_3$, CeS, and Ce_2O_2S multiphase inclusions appears in steel. When 0.011 wt.% < W ([Ce]) $\leq$ 0.016 wt.%, the spherical-shaped multiphase inclusions containing $CeAlO_3$ and Ce_2O_2S can be obtained, but, at the same time, CeS and MnS inclusions do not appear in steel. When W ([Ce]) > 0.016 wt.%, some second-phase particles containing Ce with brittleness and poor corrosion resistance appear in steel, which is not conducive to improving the corrosion resistance and the mechanical properties of steels.

3.2 Effects of Ce Addition on Microstructure and Microhardness

Figure 4 presents the microstructures of AISI 202 stainless steel. The microstructures of all steels composed of austenite and a small amount of ferrite were observed using Axiovert 25 (ZEISS) microscope. With the increasing Ce content, the grain sizes of AISI 202 stainless steels continuously were refined, and their grain shapes were changed from the long strip into elliptic-spherical shape.

As the heterogeneous nuclei concentrated on a liquid-solid two-phase interface, high melting point compounds which Ce formed can increase the nucleation rate. Although Ce can be completely dissolved in the liquid phase, its solubility in the solid phase is small because of its small equilibrium partition coefficient value. Once solidified, Ce concentrates on liquid

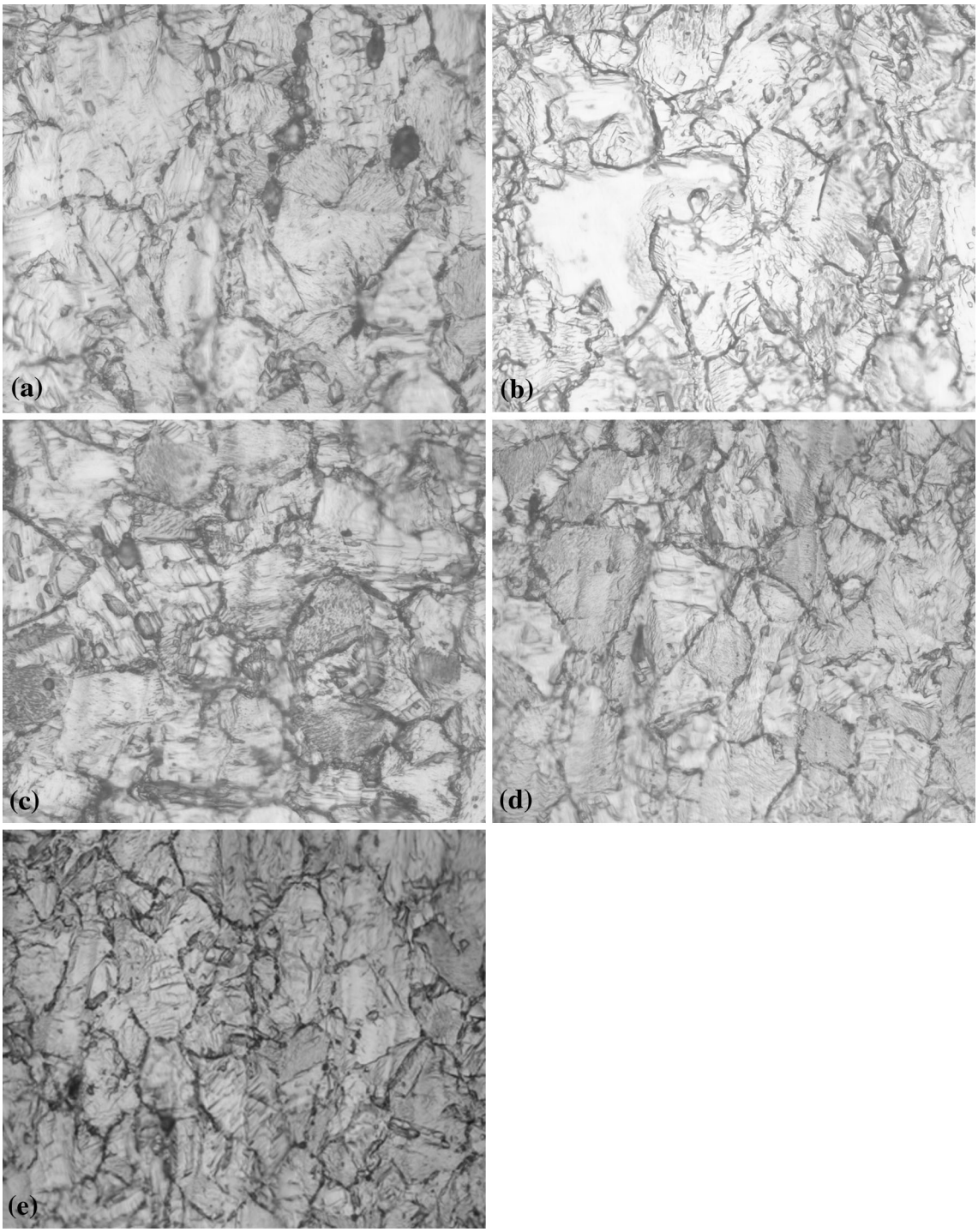

Fig. 4 Microstructures of AISI 202 stainless steel: (a) Sample A without Ce addition; (b) Sample A1 with 0.005 wt.% Ce addition; (c)

phase under crystallization, hindering the solid phase from getting the corresponding atoms from the liquid phase; consequently, the growth of grains was prevented, and the grains became finer. In addition, Ce with the surface activity can make the surface tension of steels decrease, which leads to the decrease of nucleation energy, thereby increasing the nucleation rate.

The Vickers hardness values of the five samples of AISI 202 stainless steels were measured as 202, 209, 220, 228, and 222 HV, respectively. The results indicate that the Vickers hardness values of steels increase with the increasing Ce content. When Ce content surpasses the optimized value, a large number of second-phase particles containing Ce result in the decreased values of the microhardness of steels.

When Vickers hardness was tested on materials, the surface contact of pressure head mainly had two kinds of deformation (pile-up or sink-in), as shown in Fig. 5.

A distinctive feature of indentation experiments is that the material around the contact area tends to deform upward or downward. This behavior results in piling-up or sinking-in of

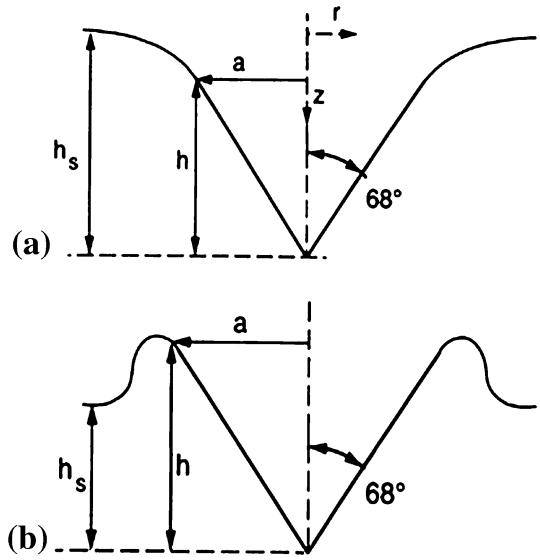

Fig. 5 Schematic of pile-up and sink-in types of material deformation around the Vickers indenter: (a) sink-in and (b) pile-up (Ref 29)

material at the contact boundary. Compared with the sink-in deformation, the pile-up deformation presents a lower strain-hardening exponent.

This surface deformation around the indent is also related to the movement of dislocations. When the dislocations move near the grain boundaries refined by Ce, the finer metal grains produce huge barriers, causing the release of the plastic deformation energy. Moreover, the dislocation piling-up occurs at grain boundaries caused by the pinning effect of Ce, thereby affecting its deformation behavior. As a surface-active element, in the process of crystallization, Ce atoms along the grain boundary can lower the nucleation energy and promote the spontaneous nucleation during the solidification, and as a result, the grains are refined. Consequently, Ce can not only improve the strength, but can also increase the plasticity of steels, thereby resolving the contradiction between the strength and plasticity.

Figure 6 depicts the microhardness indentation morphologies of AISI 202 stainless steel. The microhardness indentation morphologies of samples A and A1 with higher strain-hardening exponents presented the sink-in deformation, as shown in Fig. 6(a) and (b). Clearly, the microhardness indentation

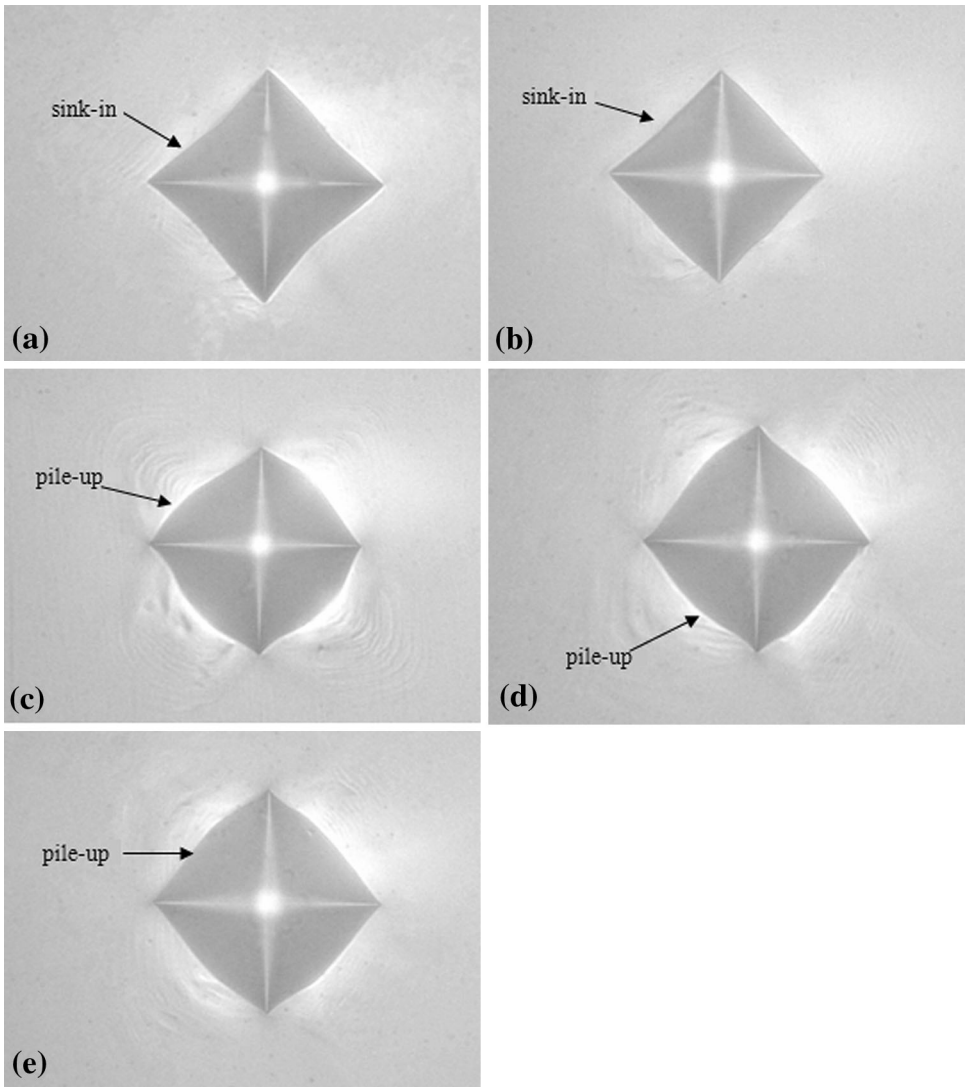

Fig. 6 Microhardness indentation morphologies of AISI 202 stainless steel: (a) Sample A without Ce addition; (b) Sample A1 with 0.005 wt.% Ce addition; (c) Sample A2 with 0.011 wt.% Ce addition; (d) Sample A3 with 0.016 wt.% Ce addition;(e) Sample A4 with 0.022 wt.% Ce addition

morphologies of samples A2, A3, and A4 with lower strain-hardening exponents showed the pile-up deformation, which meant that their brittleness was lower than those of samples A and A1, illustrating that they had better formability. Upon increasing Ce addition, the indentation morphology of samples transferred from sink-in types to pile-up types, which illustrated that the samples containing Ce had good machinability.

As is well known, after cold working, the strain-hardening exponent of AISI 202 stainless steel rises sharply ($n > 15$), resulting in the processing difficulties. The segregation of Ce atoms along the grain boundary is helpful in improving interaction with other elements, thereby affecting nucleation and development of new phases, eventually changing the microstructure and properties of steel. A moderate amount of Ce can strengthen the grain boundary and hinder propagation of intergranular cracks, improving the formability, and the brittleness at room temperature.

3.3 Tensile Test

Figure 7 presents the tensile curve of AISI 202 stainless steels at room temperature. It fully confirms that the tensile strength of sample A without Ce was far lower than that of others.

The values of tensile strength, yield strength, elongation, the reduction of area, and yield ratio are presented in Table 3. Clearly with the increasing Ce content, their yield ratios decreased. In contrast to sample A3, the yield ratio of sample A4 showed a significant reduction, which meant that the reliability of the steel decreased.

As shown in Table 3, after adding Ce, the tensile strength and the yield strength of steels were improved substantially. Compared with sample A, the elongations of other samples increased by 3.2, 5.48, and 6.45%, respectively. Obviously, their reductions in areas were also accompanied by increases of 4.5, 6.38, and 12.5% respectively; in contrast, the one of sample A4 declined slightly. For AISI 202 stainless steels added with Ce, their tensile strengths and yield strengths had a marked improvement, and the values of elongation and the reduction of area were the greatest when 0.016 wt.% Ce was added into the steel, indicating that sample A3 had the best processing performance.

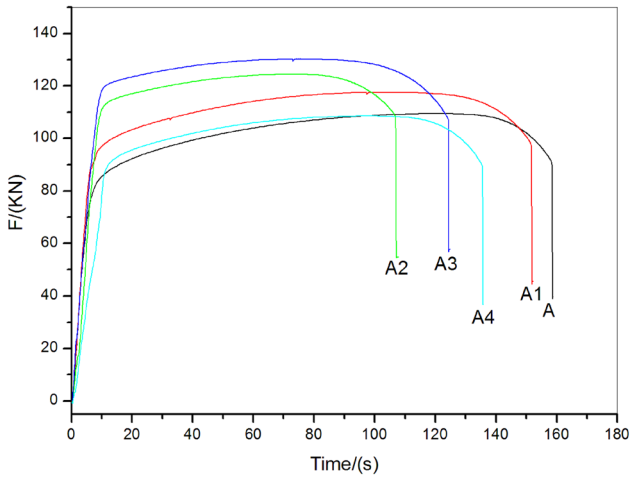

Fig. 7 Tensile curves of AISI 202 stainless steels at room temperature

Tensile test results illustrate that sample A without Ce has a minimum strength and less plasticity, and a reasonably moderate amount of Ce not only plays an important role in improving the strength, but also in effectively improving the plasticity, and thus results in improving the formability of steels. Ce can effectively modify inclusions: change irregular shape into spherical one and make them finer, and then reduce the source of cracks, which not only increases the strength, but also effectively improves the plasticity. When the appropriate amount of Ce is added into the steel, the sulfides are dispersed as small spherical particles into steel, improving the state of grain boundary to be further purified and strengthened, which leads to the improvement of mechanical properties.

A series of strength indexes resisting plastic deformation ability of metal material are determined by the material's resistance to the dislocation motion. The mutual motion of a certain amount of solute atoms and dislocations can strongly influence the strength of materials, especially for alloying elements having the lower solubility. Ce in solid-solution exists in the defects of grain boundaries or dislocation; thus, in plastic deformation process of steels, the increases in the resistance of grain boundaries and dislocation motion result in improving the strength and the microhardness.

As shown in Fig. 8 and 9, judging from SEM morphologies of tensile fractures, the macro-fractographic appearance of sample A with a large cavity band and large-scale deformation band was coarser, and its whole fracture belonged to the typical intergranular fracture mode. Some intergranular secondary cracks appeared on the fracture, which meant the existence of impurity elements in grain boundaries. The grain boundary strength was reduced, and the samples attained easy-to-fracture tendency to form the extension of cracks along the grain boundary and result in the intergranular fracture. The fracture of sample A1 with tiny and uniform dimples was transformed from the manner of intergranular brittle fracture to the manner of intergranular brittle fracture with dimple gliding fracture. The fracture morphology of sample A2 on a macroscopic scale was cup shaped and had features of ductile fracture on the microscopic scale. It was observed that the fiber zone in sample A2 showed fracture with multiple large-sized equiaxed dimples. There were fiber zone and shear lip zone in sample A3 instead of radial zone, and the equiaxed dimples of the fracture became larger and shallower. With regard to sample A4, there were some

Table 3 Tensile results of AISI 202 stainless steel at room temperature

Simple	Tensile strength, MPa	Yield strength, MPa	Elongation, %	Reduction of area, %	Yield ratio
A	1090	996	62.1	48.9	0.914
A1	1170	1011	64.0	51.1	0.864
A2	1230	1052	65.4	52.3	0.855
A3	1300	1108	66.2	55.2	0.852
A4	1070	974	64.3	51.5	0.910

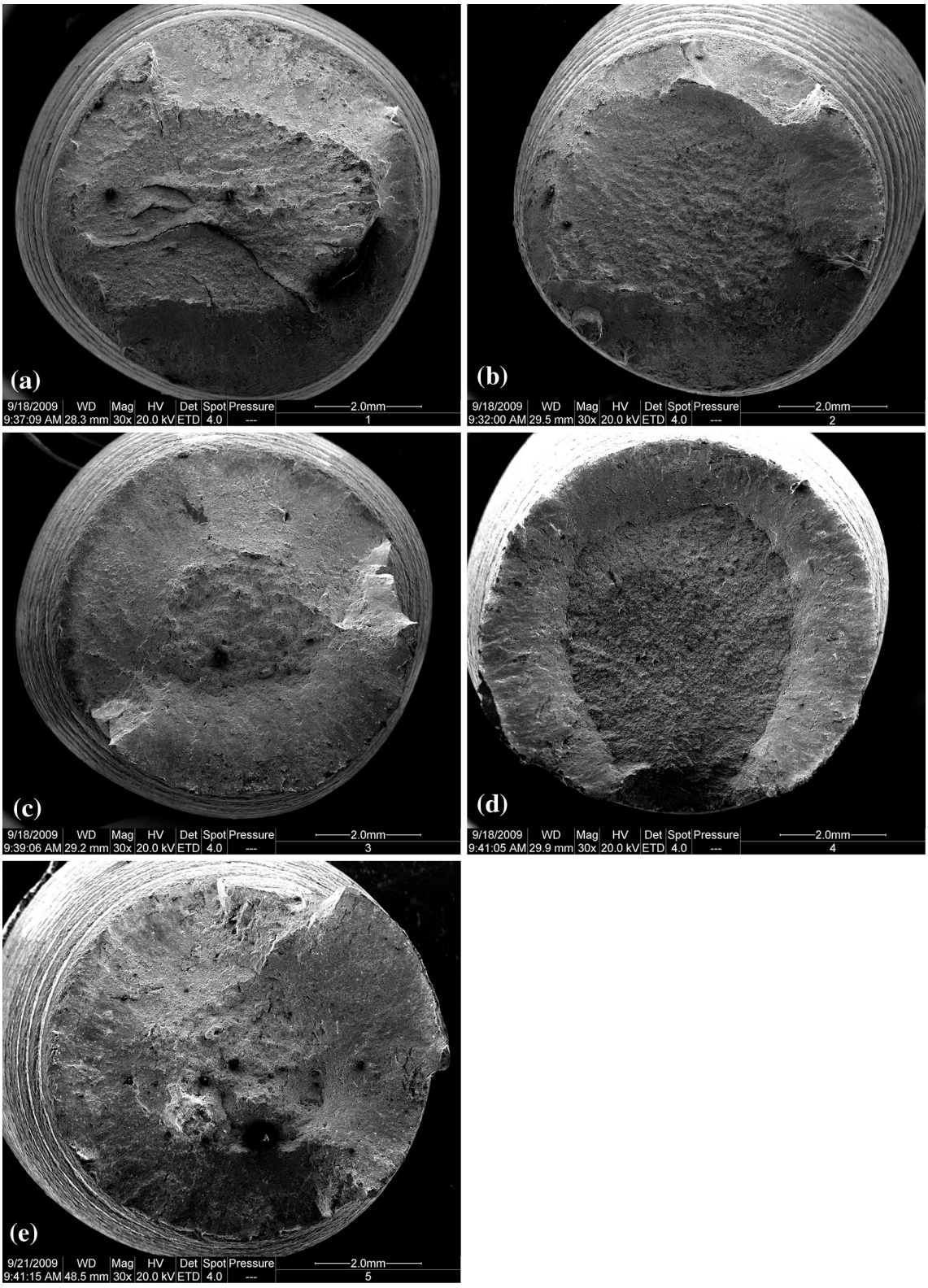

Fig. 8 Macrofractographic appearance of AISI 202 stainless steel from tensile test: (a) Sample A without Ce addition; (b) Sample A1 with 0.005 wt.% Ce addition; (c) Sample A2 with 0.011 wt.% Ce addition; (d) Sample A3 with 0.016 wt.% Ce addition; (e) Sample A4 with 0.022 wt.% Ce addition

tiny spherical inclusions with dimples at the bottom of fracture. These inclusions correspond to $CeAlO_3$ and Ce_2O_2S multiphase inclusions according to the energy spectrum (Fig. 10), occurring due to the excessive Ce content in steel.

Very large strips of MnS and Al_2O_3 nonmetallic inclusions exist in sample A without Ce, forming pores and microcracks on the fracture surface, and hence, its tensile property was not very ideally favorable. Further, after adding Ce, the effects of

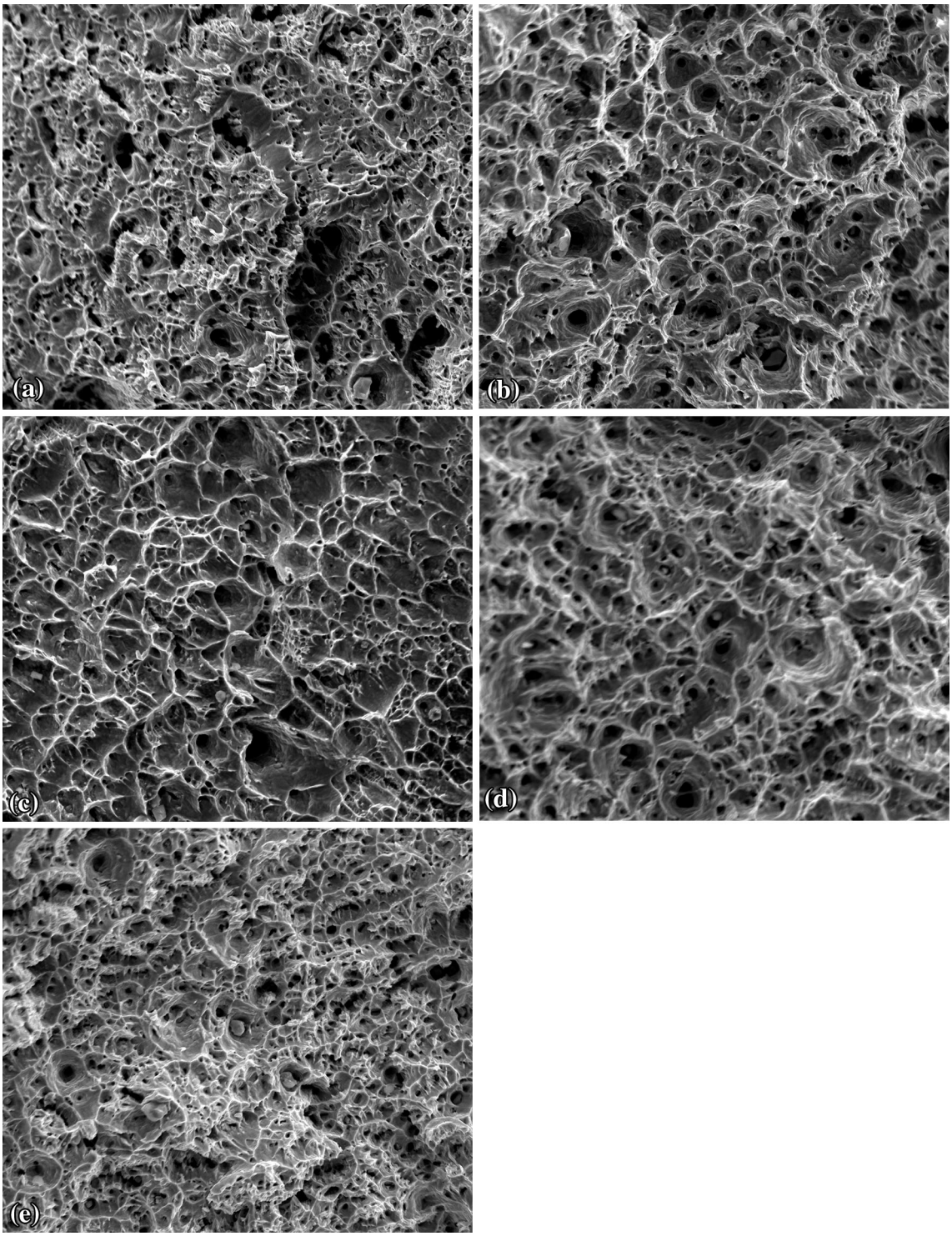

Fig. 9 SEM micrographs of tensile fractures: (a) Sample A without Ce addition;(b) Sample A1 with 0.005 wt.% Ce addition; (c) Sample A2 with 0.011 wt.% Ce addition; (d) Sample A3 with 0.016 wt.% Ce addition; (e) Sample A4 with 0.022 wt.% Ce addition

Ce on purifying grain boundary, inclusions removal, and modifying inclusions, made the equiaxed dimples become larger and deeper on the fracture; as a result, the tensile properties of steels were significantly improved. However, sample A4 with excessive Ce produced a large number of second-phase inclusions. They occurred in a large number of equiaxed dimples, which was not conducive to improve the mechanical properties of steels.

The fracture mode of AISI 202 stainless steel added with Ce belongs to ductile fracture originating from the inclusion/matrix interface. The appropriate content of Ce added into the steels can delay the initiation and rupture of cracks, forming large and

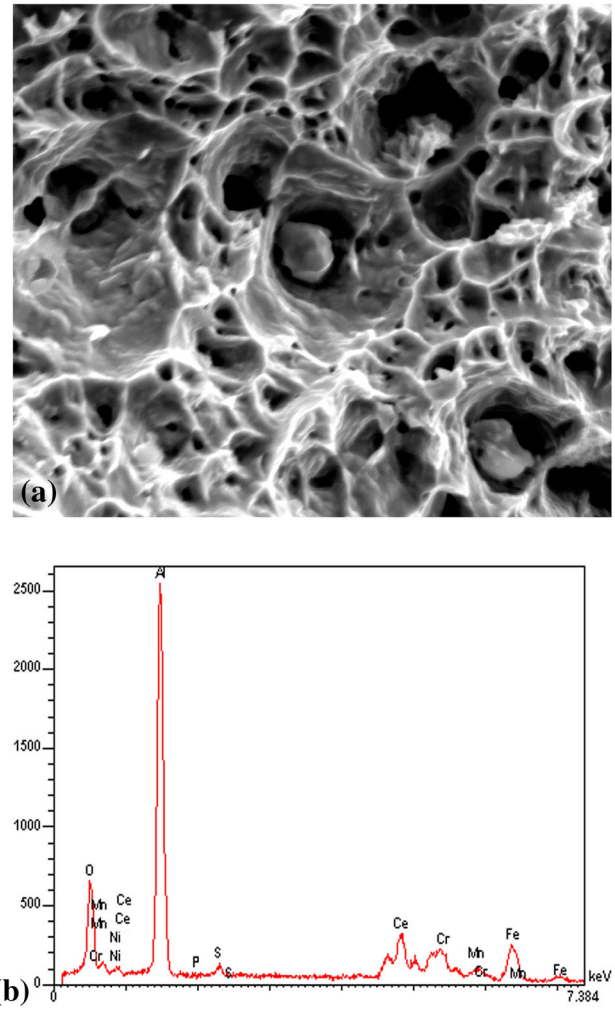

Fig. 10 Inclusions in sample A4 and its energy spectrum

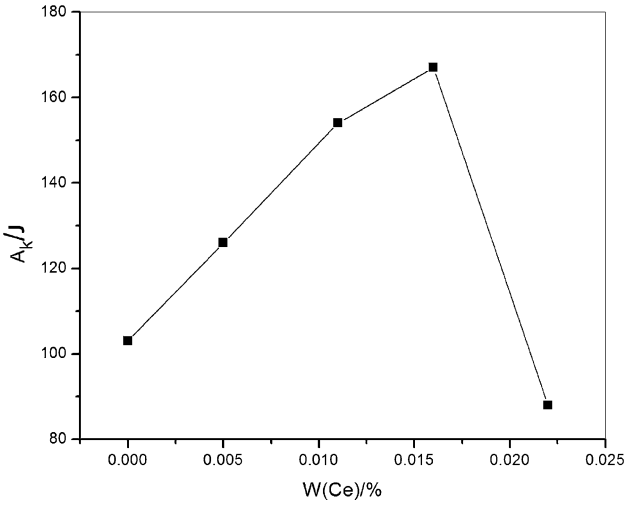

Fig. 11 Relationship between Ce content and impact toughness

deep equiaxed dimples, which makes the plasticity in the fracture improve significantly, thereby effectively improving the mechanical properties of steel. In addition, when the dislocations move near the grain boundary refined by Ce, the finer metal grains produce huge barriers, improving the strengthening effect of AISI 202 stainless steel.

3.4 Impact Toughness

Figure 11 presents the relationship between Ce content and impact toughness. Compared with sample A, the A_k values of other steels added with an appropriate amount of Ce increased by 62.1, 49.5, and 22.3%, respectively. Therefore, the impact toughness of steels was improved upon increasing the Ce content. In contrast to sample A3, the impact toughness of sample A4 decreased by nearly half.

The solid-solution of Ce in grains can not only increase diffusion activation energy of crystal interfaces, but also improve the moving resistance of grain boundary and dislocations, which leads to the improvement of impact toughness (Ref 30). In addition, Ce refines the sizes of grains. Grain refinement can improve the strength as well as the toughness; thus, the impact toughness of the steel is improved. After Ce concentration surpasses the optimal value in steel, the Ce-contained inclusions with a high melting point grow up into large-sized brittle second-phase particles with a low melting point, precipitating along the grain boundaries, which will cause hot brittleness of the steel.

As shown in Fig. 12, when observing the impact fracture of AISI 202 stainless steel, sample A without Ce had an irregular macrofracture where the radial zone accompanied by several significant cracks appeared. These extending cracks were interconnected under the influence of outside force. No sign of plastic deformation could be observed on the fracture surface; rod-like nonmetallic inclusions composed of MnS and Al_2O_3 existed in the fracture, and very easy to lead to the brittle fracture. The macrofractographic appearance of sample A1 basically presented the characteristics of dimple fracture. Its impact fracture featured a transgranular quasi-cleavage consisting of clear tearing ridges and tiny quasi-cleavage planes, and its shear lip area had a few uneven shallow dimples. As shown in Fig. 13, the whole fracture of sample A2 featured the mode of the dimple fracture. Its surface cracks were in the form of porous aggregates extending from the section near the center to the outer side, and some large-sized equiaxed dimples existed in the fracture. A typical dimple fracture mode occurred on the macrofracture of the sample A3 where its equiaxed dimples became larger and deeper. As shown in Fig. 14, with regard to the fracture of sample A4, there were some small second-phase particles less than 5 μm in size at the center of dimples, which indicated Ce could make inclusions smaller and finer in matrix. However, the excessive Ce existed in sample A4; consequently, the plasticity of fracture decreased significantly.

After the addition of the appropriate amount of rare earth Ce, in the plane perpendicular to the stress, the rate at which micropores grow in all directions is equal. The distribution of stress on the entire fracture is thus uniform, which is helpful in the formation of uniform equiaxed dimples. The cracks often occur in the weakness of grains such as the precipitates, inclusions/matrix interface, grain boundary positions, etc., however, a proper amount of Ce effectively prevents cracks from propagating. The higher impact energy can be obtained when the fracture surface has larger fraction of shear lips and fiber region with bigger and more homogeneous dimples. With regard to the fracture of steels with Ce, the large fiber region presents larger and uniform equiaxed dimples, and

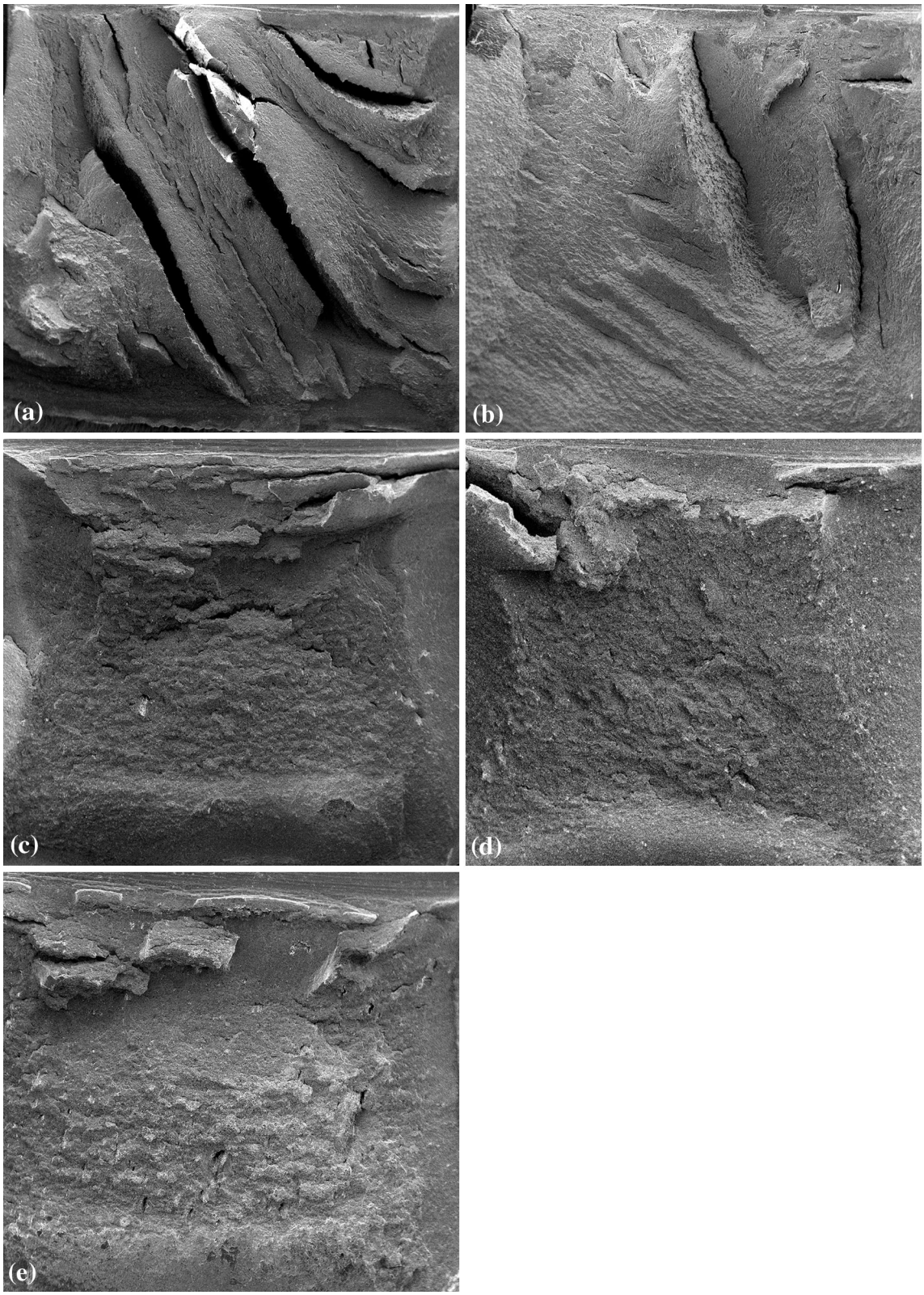

Fig. 12 Macrofractographic appearance of AISI 202 stainless steel from impact test: (a) Sample A without Ce addition; (b) Sample A1 with 0.005 wt.% Ce addition; (c) Sample A2 with 0.011 wt.% Ce addition; (d) Sample A3 with 0.016 wt.% Ce addition; (e) Sample A4 with 0.022 wt.% Ce addition

the transition of fracture morphology occurs from intergranular fracture to transgranular fracture, thereby effectively improving the impact toughness of steels.

As a surface-active element, in the process of crystallization, Ce atoms along the grain boundary decrease the nucleation energy during the solidification, increase the

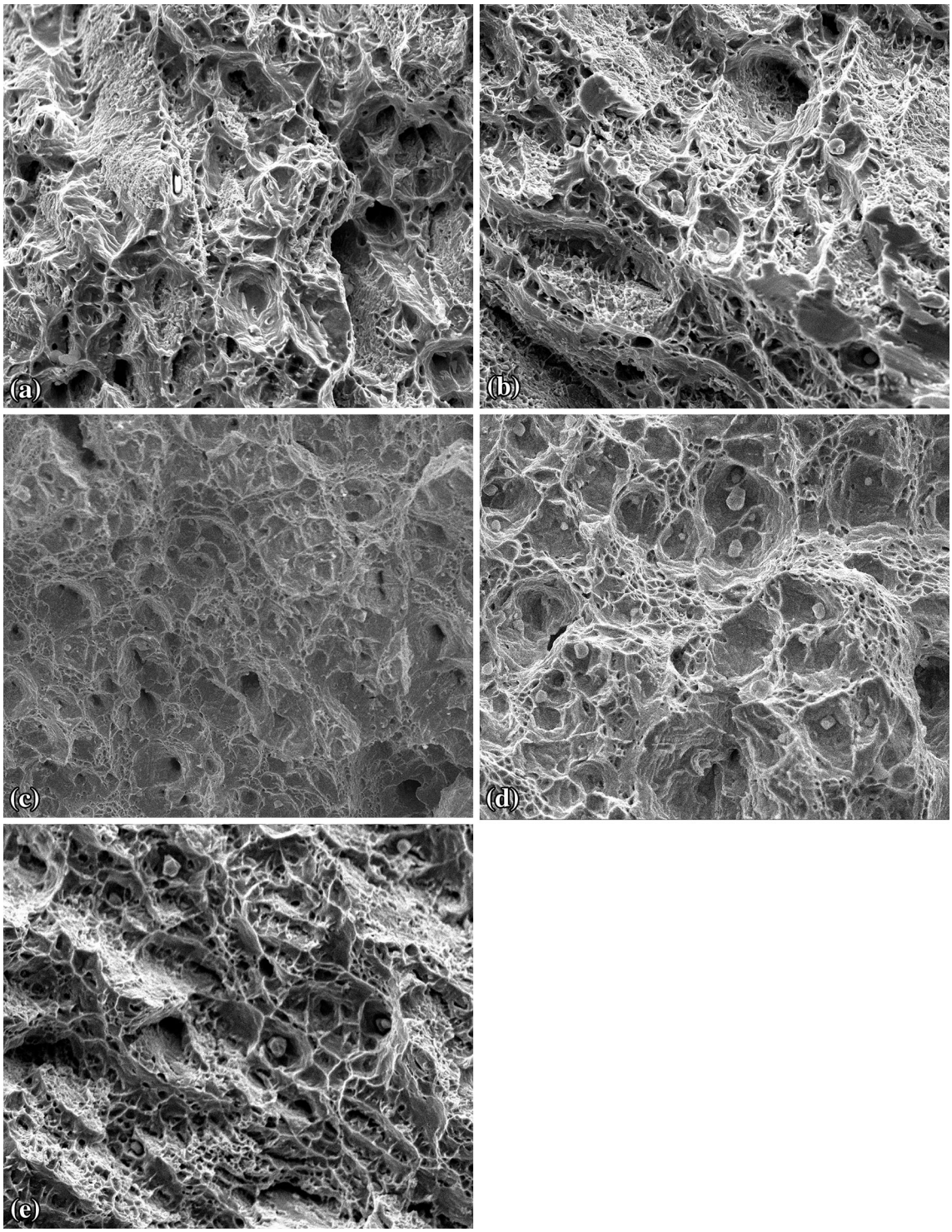

Fig. 13 SEM micrographs of impact fractures: (a) Sample A without Ce addition; (b) Sample A1 with 0.005 wt.% Ce addition; (c) Sample A2 with 0.011 wt.% Ce addition; (d) Sample A3 with 0.016 wt.% Ce addition; (e) Sample A4 with 0.022 wt.% Ce addition

nucleation rate, promote the spontaneous nucleation, and the grains become refined. Consequently, the refinement of grains significantly increases the strength; in the meantime, its plasticity is improved, resolving the contradiction between the strength and plasticity of steels. However, the excessive Ce can produce some brittle second-phase particles containing Ce, destroying the continuity of the matrix, and then the lattice distortion occurs in the second-phase particles or around the matrix, thereby affecting its fracture behavior. In contrast, the intensity of second-phase particles is higher than that of the matrix, so the lattice distortion is mainly focused on the matrix around the second-phase particles, thereby forming the high-energy region, which leads to a decline in its mechanical properties.

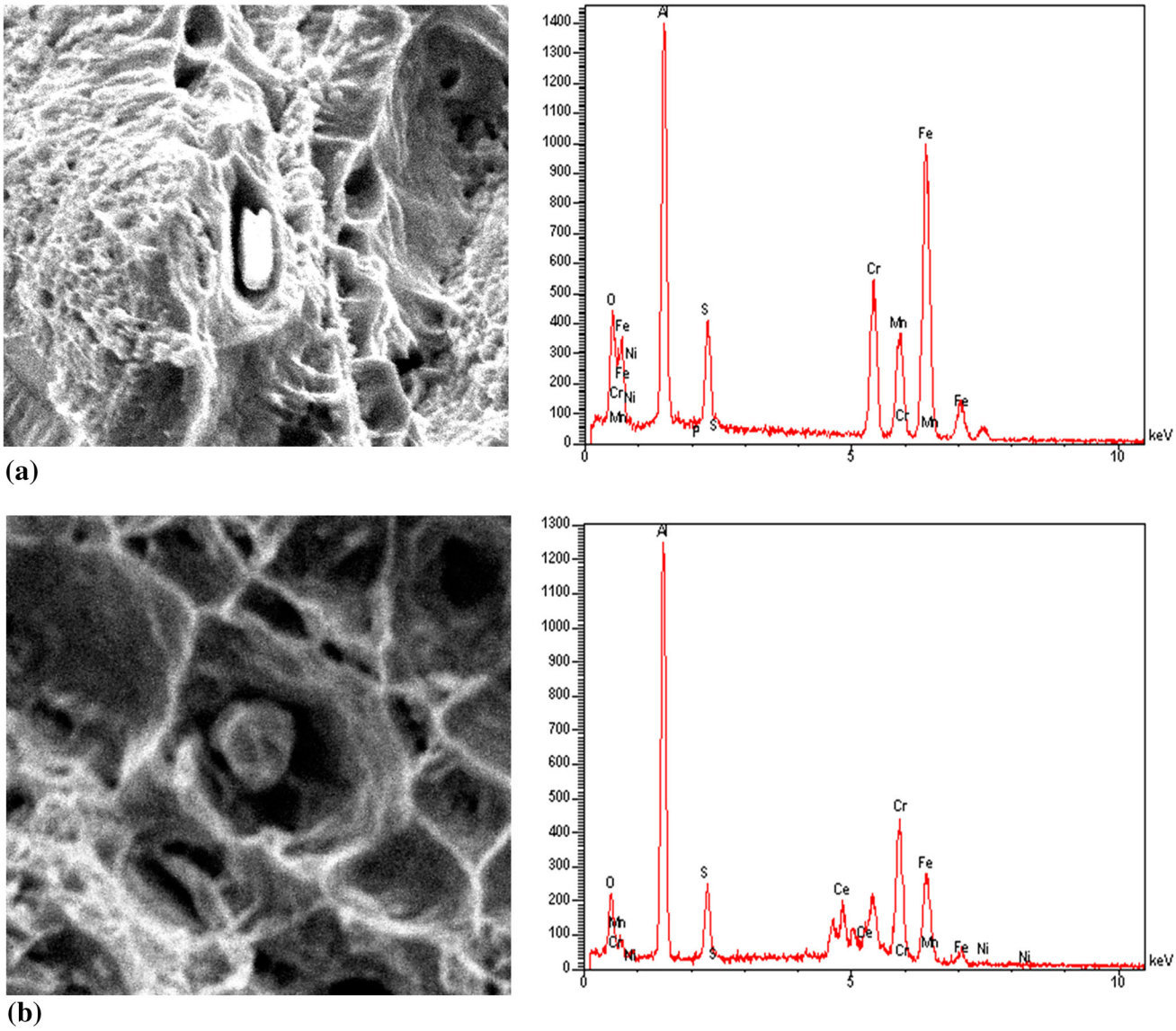

Fig. 14 Inclusions on the impact fracture: (a) Sample A without Ce addition and (b) Sample A4 with 0.022 wt.% Ce addition

Table 4 Weight loss rates at different immersion times (gmm^2/days)

	Immersion time, days		
Sample	**15 d**	**30 days**	**45 days**
A	235	63.5	128
A1	88.3	42.9	115
A2	59.8	28.6	31.4
A3	22.3	17.3	25.2
A4	46.7	25.7	78.5

3.5 Corrosion Behavior in 5 wt.% H_2SO_4 Solution

Effects of Ce addition on corrosion behavior were studied in 5 wt.% H_2SO_4 solution, and the times of cycle immersion test were 15, 30, and 45 days, respectively. The weight loss rates of experimental steels are presented in Table 4.

As presented in Table 4, the corrosion rate of sample A was greater than that of others. In contrast, sample A3 was corroded at the minimum rate. Owing to the faster rate of corrosion on the matrix surface in the initial stage, Ce added into steel delayed the uniform corrosion rate of AISI 202 stainless steel. The corrosion rates of all steels were lower on day 30 because the corrosion products constantly deposited on the matrix surface with time, and the generation of rust layer thickening further improved the corrosion resistance. The corrosion rate rose again on day 45 when the binding force close to the rust layer gradually reduced to a certain degree. The outermost rust layer was out of the whole rust layer, thereby reducing the rust layer thickness. However, the protective rust layer falling off increased the corrosion rate of steel. With the increasing Ce content, the protective rust layer enhanced uniform corrosion resistance and reduced the corrosion rate of AISI 202 stainless steel.

Figure 15 presents EIS values of AISI 202 stainless steel in 5 wt.% H_2SO_4 solution with different immersion times. In 5 wt.% H_2SO_4 solution, the uniform corrosion occurred on the

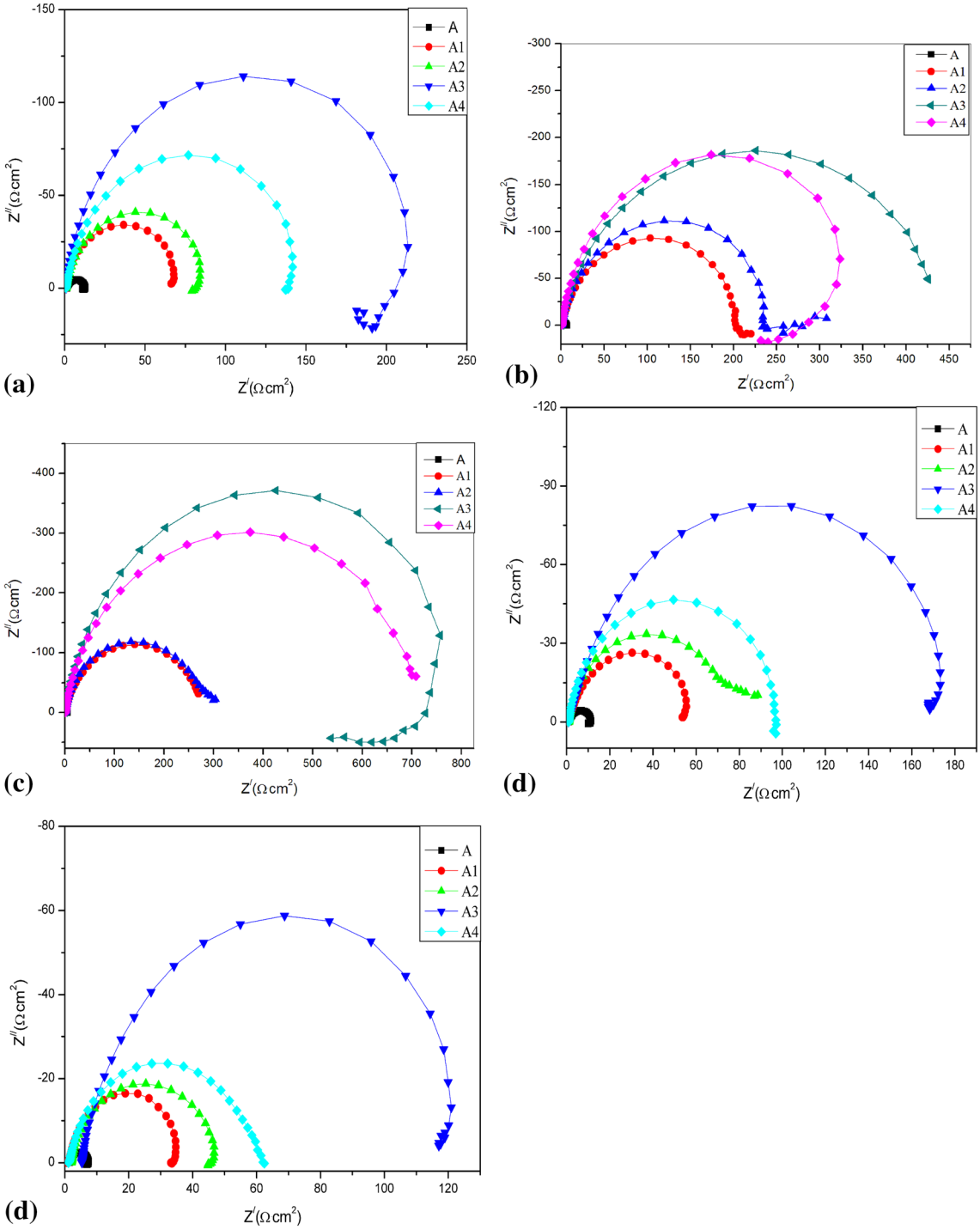

Fig. 15 EIS of AISI 202 stainless steel in 5 wt.% H_2SO_4 solution with different immersion times: (a) for 1 day; (b) for 5 days; (c) for 15 days; (d) for 30 days; (e) for 45 days

Table 5 Tafel results on day 1

Sample	B_a, mV	B_c, mV	I_{corr}, Amp/cm	E_{corr}, Volts	R_p, Ω
A	83.812	75.12	5.6116×10^{-3}	−0.41003	4.6487
A1	94.919	87.819	7.9742×10^{-4}	−0.38469	32.71
A2	117.69	99.604	5.8152×10^{-4}	−0.37394	44.86
A3	124.52	116.95	1.6956×10^{-4}	−0.31937	101.59
A4	121.32	108.43	2.1288×10^{-4}	−0.35618	72.53

Table 6 Tafel results on day 15

Sample	B_a, mV	B_c, mV	I_{corr}, Amp/cm	E_{corr}, Volts	R_p, Ω
A	117.69	108.43	2.8329×10^{-3}	−0.38893	9.2087
A1	129.79	122.14	4.0511×10^{-4}	−0.37726	142.73
A2	134.11	130.81	3.9324×10^{-4}	−0.34817	145.55
A3	156.22	150.97	7.2352×10^{-5}	−0.31026	365.56
A4	141.69	141.66	7.5342×10^{-5}	−0.34151	346.25

Table 7 Tafel results on day 45

Sample	B_a, mV	B_c, mV	I_{corr}, Amp/cm	E_{corr}, Volts	R_p, Ωs
A	97.36	78.19	3.2769×10^{-3}	−0.43036	7.9632
A1	111.86	101.57	8.2327×10^{-4}	−0.40324	17.56
A2	125.23	107.28	6.2915×10^{-4}	−0.38729	23.42
A3	136.21	128.53	5.3264×10^{-4}	−0.35794	59.39
A4	122.71	113.57	7.8571×10^{-4}	−0.39628	31.68

stainless steel surface (Ref 31). It was clear that the capacitance loops of all steels were complete, but their radii were different. AC impedance of sample A without Ce had the smallest radius of the capacitance loop, corresponding to the smaller polarization resistance (R_p) value, which meant at the faster corrosion rate, the uniform corrosion of AISI 202 stainless steel without Ce was severely affected in 5 wt.% H_2SO_4 solution.

The radius of capacitance loop of sample A was much smaller than that of others on day 1. All radii of capacitance loops were accompanied by an increasing Ce content. To sample A4, its radius of the capacitance loop was smaller than that of sample A3, which illustrated the excessive Ce was not conducive to improve the uniform corrosion resistance of AISI 202 stainless steel. With the increasing time, with respect to other samples, their radii of capacitance loops increased initially, and then reduced; however, the one of sample A remained at the minimum value.

Corrosion products were formed in nonmetallic inclusions (Ref 32). When the diffusion velocity was more than the deposition rate, most of the corroded products were diffused on the surface of steel, and thus reduced its potential (Ref 33). The diffusion velocity of corrosion products had a sharp slowdown because the corrosion products were deposited continuously to form a good adhesion rust layer delaying the corrosion rate on day 15.

Up to 30 days, all radii of capacitance loops decreased gradually; in the meantime, the porous outer rust layer was formed out of the protective rust layer; as a result, the thickness of protective rust layer decreased. The decrease of R_p values significantly increased electrochemical reaction rate, which led to the formation of uniform corrosion and a huge loss of quality. By contrast, to sample A3 with 0.016 wt.% Ce addition, its radius of the capacitance loop did not decrease significantly.

A moderate amount of Ce can enhance the adhesion between the rust layer and the steel matrix, which results in the generation of dense rusty layer (Ref 34), thereby greatly improving the uniform corrosion resistance of AISI 202 stainless steel. The uniform corrosion in 5 wt.% H_2SO_4 solution presents very small cathodic and anodic area of corrosion battery, and the location of the cathode and anode is constantly changing (Ref 35). The whole surface of steels is in the active state, only various points have a large energy fluctuation with time. The anode is in high energy and the cathode is in low energy (Ref 36), consequently, the uniform corrosion appears on the entire surface of the stainless steel. From the micro perspective, numerous micro cells form on the surface of matrix, the reaction equations are described as follows:

$$M \rightarrow M^{n+} + ne \text{ (micro anode)} \quad \text{(Eq 8)}$$

$$2H^+ + 2e \rightarrow H_2 \text{ (micro cathode)} \quad \text{(Eq 9)}$$

When the metal is corroded in non-oxidative acid solutions without dissolved oxygen, the compact passive film does not exist on its surface, which generally belongs to the control system under activated control. At this point, the only depolarizer is H^+ ions in solution, and the cathodic and anodic reactions are controlled by activation polarization.

In the Table 5, b_a and b_c show the Tafel slopes of the anodic reaction and cathodic reaction, respectively.

Tables 5, 6, 7 present Tafel results of AISI 202 stainless steel in 5 wt.% H_2SO_4 solution. With respect to sample A4, R_p values increased gradually upon increasing the Ce content, and their corrosion resistance became better and better. Obviously, R_p value of sample A4 was less than that of sample A3, which indicated that the excessive Ce decreased the uniform corrosion resistance of AISI 202 stainless steel.

R_p presents the value of the polarization resistance. The greater R_p value means the migration of charges is difficult, and the uniform corrosion does not occur easily. The corrosion potential (E_{corr}) becomes larger, and the corrosion current density (i_{corr}) decreases as the Tafel slope's b_a and b_c values of steel gradually increase, which leads to the better corrosion resistance of steel.

As shown in Tables 5, 6, 7, both the Tafel slope's b_a and b_c values of sample A without Ce were minimum, and it was most likely to be corroded. Compared with other steels, both the Tafel slope's b_a and b_c values of sample A3 were maximum; obviously, this sample had the best uniform corrosion resistance. However, the i_{corr} value of sample A4 was significantly higher than that of sample A3, which meant excessive amount of Ce caused the uniform corrosion resistance of the steel to decrease.

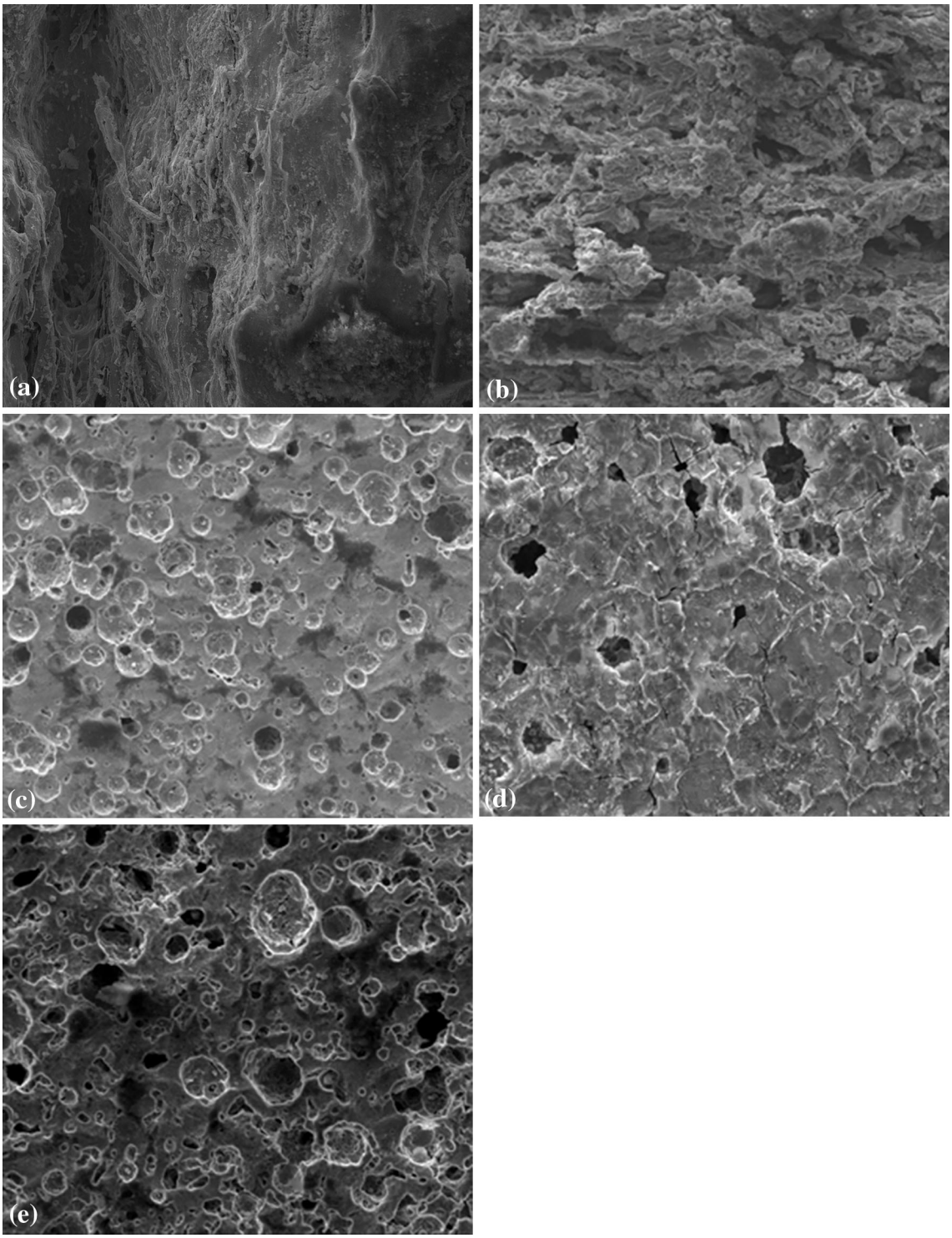

Fig. 16 SEM morphology of AISI 202 stainless steel after 45 days: (a) Sample A without Ce addition; (b) Sample A1 with 0.005 wt.% Ce addition; (c) Sample A2 with 0.011 wt.% Ce addition; (d) Sample A3 with 0.016 wt.% Ce addition; (e) Sample A4 with 0.022 wt.% Ce addition

Because the whole metal surface is in active state in 5 wt.% H_2SO_4 solution, only various points have a large energy fluctuation over time, so it can not form the complete passive film and passivation region. Under the same potential, the i_{corr} values of others are always smaller than that of sample A, and with the increasing Ce content in steel, i_{corr} decreases continuously.

Ce with high activity and electrochemical electrode potential can make polarization resistance increase, and shift the anodic polarization potential to positive value (Ref 37), reduce the corrosion rate, delay the process of corrosion, and improve the corrosion resistance of steel. However, when adding the excessive Ce, some second-phase particles containing Ce with

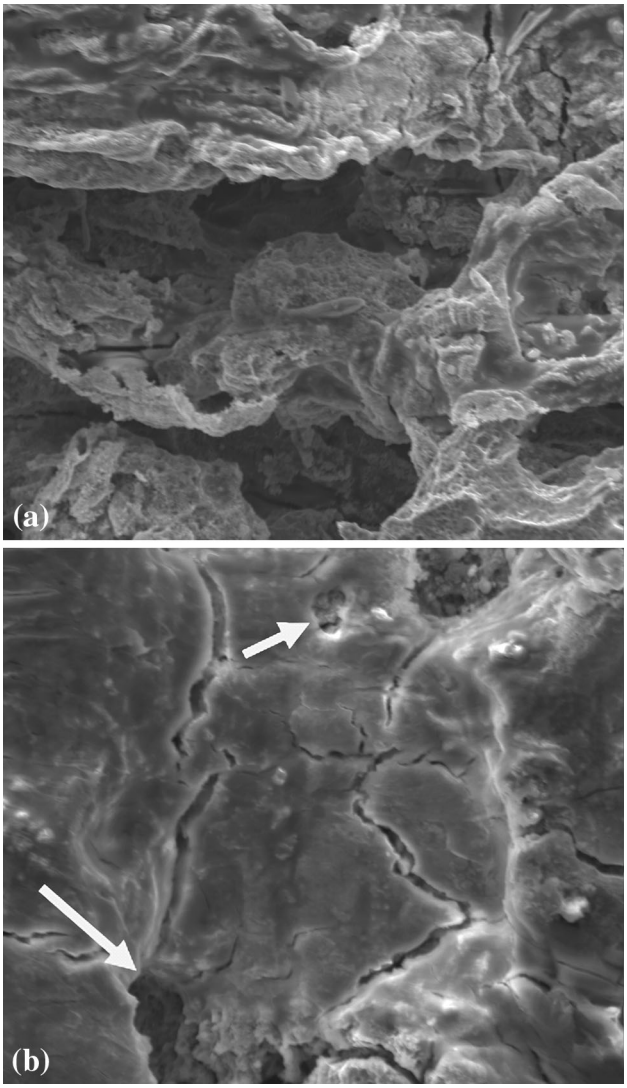

Fig. 17 SEM micromorphology of AISI 202 stainless steel after 45 days: (a) Sample A without Ce addition and (b) Sample A3 with 0.016 wt.% Ce addition

poor corrosion resistance will exist in steel, which is not conducive to improving its uniform corrosion resistance.

3.6 Corrosion Mechanism

This research adopts the method of constant potential, and the electrochemical polarization curves were measured in weak polarization region to discuss the influence of Ce on the corrosion resistance of AISI 202 stainless steel.

The corrosion behavior in 5 wt.% H_2SO_4 solution of the stainless steel belongs to the hydrogen evolution corrosion. The metal electrode potential ($E_{M^{n+}}$) must be lower than the hydrogen electrode potential (E_{H_2}):

$$E_{M^{n+}} < E_{\mathrm{H}_2}, \quad \text{(Eq 10)}$$

where E_{H_2} is equal to the difference between the hydrogen balance potential (E_{e,H^+}) and the overpotential of hydrogen evolution (η_{H_2}):

$$E_{\mathrm{H}_2} = E_{e,H^+} - \eta_{\mathrm{H}_2}, \quad \text{(Eq 11)}$$

According to Nernst equation, E_{e,H^+} is defined as

$$E_{e,H^+} = E^{\Theta}_{e,H^+} + \frac{2.3RT}{F}\lg a_{H^+} = -0.059\mathrm{PH}\ . \quad \text{(Eq 12)}$$

So the conditions of the hydrogen evolution corrosion are as follows:

$$E_{M^{n+}} < -\left(0.059\mathrm{PH} + \eta_{\mathrm{H}_2}\right). \quad \text{(Eq 13)}$$

Most of hydrogen evolution corrosion is the corrosion process of cathode and anode hybrid control (Ref 38). The stainless steel in dilute acid controlled by anodic process is a kind of hydrogen evolution corrosion (Ref 39). In this case, the metal ions with a high anodic polarization must penetrate the passive film to enter the solution. Appropriate content of Ce can reduce cathodic inclusions with small overpotential of hydrogen evolution, changing them into the inclusions containing Ce, which have a large overpotential of hydrogen evolution (Ref 40). Consequently, the corrosion effect of inclusions is weakened, and the corrosion rate is delayed. A compact passive film exists on the surface of AISI202 stainless steel in the air; however, after being immersed in 5 wt.% H_2SO_4 solution, the passive film will soon dissolve, and eventually disappear, forming active metal surface. At this point, the cathodic reaction and the anodic reaction are controlled by activation polarization.

3.7 Morphologies of Rust Layers

Figure 16 depicts SEM morphology of AISI 202 stainless steel in 5 wt.% H_2SO_4 solution after 45 days. In contrast to other steels, the rust layer of sample A without Ce was particularly loose and porous, and a deep longitudinal crack appeared on its surface. Obviously, corrosion products had not protected the matrix. Corrosive ions could pass through the cracks into the matrix surface. In contrast, the corrosion degree of sample A1 had been greatly improved although its fragmented rust layer was loose. A compact rust layer was observed on the surface of sample A2; in the meantime, different sizes of cracks and holes existed in local, rendering small molten-bead particle morphology, as shown in Fig. 16(c). As presented in Fig. 16(d), the thinnest rust layer and uniform corrosion occurred in sample A3. It could be seen clearly that a few gaps and holes occurring on the flake rust layer combined closely, a hole formed due to desquamating of carbide between the middle and top rust layers. By comparison, a loose and porous rusty layer appeared on the matrix of sample A4 with the excessive Ce. As a result, the uniform corrosion resistance of AISI 202 stainless steel decreased.

Figure 17 presents SEM micromorphology of AISI 202 stainless steel after 45 days. There was a severe corrosion on the surface of sample A. A large number of holes attracting each other combined to form several large corrosive holes, losing their characteristics of regular geometry. To sample A3, it was clear that a large groove occurred on the grain boundary (shown as long arrow) due to the fall-off of carbides. In the meantime, many larger corrosive pits existed in the grain inner (shown as short arrow).

Trace Ce can make the rust layer dense and enhance the adhesion ability between the rust layer and steel matrix. In addition, the process of corrosion controlled by hydrogen evolution firstly occurs in the inclusions with low hydrogen overpotential. In this case, the more the number of inclusions, the greater the dispersion, and the severer the corrosion. Suitable amount of Ce can effectively control the number of

inclusions, thereby reducing the area of active cathodic phase and increasing the degree of cathodic polarization; as a result, the cathodic process is prevented, and the uniform corrosion resistance of AISI 202 stainless steel is improved comprehensively.

4. Conclusions

1. Ce addition to AISI 202 stainless steel increased the corrosion resistance owing to metamorphic inclusions and the improvement of electrode potential in matrix. The appropriate amount of Ce effectively modified various features of inclusions, such as their quantity, size, nature, shape, and distribution, thereby transferring finer metamorphic inclusions from the grain boundary into the intragranular, to a certain extent, purified the alloy.
2. When W ([Ce]) $\leq$ 0.011 wt.%, sulfide inclusions could be controlled, and the cluster of MnS, $CeAlO_3$, CeS, and Ce_2O_2S multiphase inclusions occurred in steel. With 0.011 wt.% $<$ W ([Ce]) $\leq$ 0.016 wt.%, the spherical multiphase inclusions containing $CeAlO_3$ and Ce_2O_2S were obtained, and at the same time, CeS and MnS inclusions did not occur in steel. With W ([Ce]) $>$ 0.016 wt.%, some second-phase particles containing Ce with poor corrosion resistance existed in steel, which was not conducive to improving its uniform corrosion resistance.
3. The size of grains was refined with the Ce addition, significantly increasing the strength, and in the meantime, its plasticity was improved, which resolved the contradiction between the strength and plasticity of steels.
4. Microhardness indentation morphologies indicated that upon increasing the Ce addition, the indentation morphology of steels transferred from sink-in types to pile-up types. Ce present in the defects of grain boundaries or dislocation strengthened the grain boundary and hindered the propagation of intergranular cracks, making the resistance of grain boundaries and dislocation motion increase, thereby improving the formability and the brittleness at room temperature.
5. The fracture of AISI 202 stainless steel added with Ce belonged to the ductile fracture mode, originating from the inclusion/matrix interface. The segregation of Ce along the grain boundary delayed the initiation and the rupture of cracks, forming larger and deeper equiaxed dimples, which effectively improved the mechanical properties of steels. The lattice distortion appeared in some brittle second-phase particles which the excessive Ce produced and resulted in a decline in its mechanical properties.
6. The corrosion morphologies of rust layers illustrated that Ce enhanced the stability and continuity of the microstructure of the inner rust layer due to its role as an element with high activity and electrochemical electrode potential binding the rust layer and matrix.
7. The mechanical properties and corrosion resistance of steels were gradually improved with the increasing Ce addition. It was found that AISI 202 stainless steel with 0.016 wt.% Ce addition in the mass fraction had the optimal mechanical properties and the uniform corrosion resistance.

Acknowledgments

This work was supported by the National Natural Science Foundation Project (Grant Nos. 51174057, 51274062), the National High Technology Research and Development Program of China (Grant No. 2012AA03A503), and the Specialized Research Fund for the Doctoral Program of Higher Education of China (Grant No. 20130042110040).

References

1. P. Seemann, S. Kurz, and P. Gümpel, Martensite Formation in a New Manganese Alloyed Metastable Austenitic Steel (AISI, 200-Series), *J. Alloy. Compd.*, 2013, **577**, p 649–653
2. V. Nemanič and J. Šetina, Evolution of Hydrogen from AISI, 200 Stainless Steel: A Study to Determine Whether It is Diffusion or Recombination Limited Process and Experimental Evidence for Strongly Bound Hydrogen, *Vacuum*, 2014, **109**, p 102–107
3. N. Mazinanian, I. Odnevall Wallinder, and Y. Hedberg, Comparison of the Influence of Citric Acid and Acetic Acid as Stimulant for Acidic Food on the Release of Alloy Constituents from Stainless Steel AISI, 201, *J. Food Eng.*, 2015, **145**, p 51–63
4. X. Shan, L.Q. Wei, P. Liu, X.M. Zhang, W.X. Tang, P. Qian, Y. He, and S.F. Ye, Influence of CoO Glass-ceramic Coating on the Anti-oxidation Behavior and Thermal Shock Resistance of 200 Stainless Steel at Elevated Temperature, *Ceram. Int.*, 2014, **40**, p 12327–12335
5. W. Chuaiphana and L. Srijaroenpramong, Effect of Welding Speed on Microstructures, Mechanical Properties and Corrosion Behavior of GTA-Welded AISI, 201 Stainless Steel Sheets, *J. Mater. Process. Tech.*, 2014, **214**, p 402–408
6. H.S. Luo and C. Zhao, Low Temperature Salt Bath Hardening of AISI, 201 Austenitic Stainless Steel, *Phys. Procedia*, 2013, **50**, p 38–42
7. M. Behpour, S.M. Ghoreishi, N. Soltani, and M. Salavati-Niasari, The Inhibitive Effect of some Bis-N, S-Bidentate Schiff Bases on Corrosion Behaviour of 304 Stainless Steel in Hydrochloric Acid Solution, *Corros. Sci.*, 2009, **51**, p 1079–1082
8. P. Prabaharan, K. Devendranath Ramkumar, and N. Arivazhagan, Characterization of Microstructure and Mechanical Properties of Super Ni 718 Alloy and AISI, 316L Dissimilar Weldments, *J. Mater. Res.*, 2014, **29**, p 3011–3023
9. J.C. Zhang, D.Y. Ding, X.L. Xu, Y.J. Gao, G.Z. Chen, W.G. Chen, X.H. You, Y.W. Huang, and J.S. Tang, Effect of Ce Addition on the Mechanical and Electrochemical Properties of a Lithium Battery Shell Alloy, *J. Alloy. Compd.*, 2014, **617**, p 665–669
10. S.H. Jeon, D.H. Hur, H.J. Kim, and Y.S. Park, Effect of Ce Addition on the Precipitation of Deleterious Phases and the Associated Intergranular Corrosion Resistance of 27Cr-7Ni Hyper Duplex Stainless Steels, *J. Alloy. Compd.*, 2015, **90**, p 313–322
11. K.L. Wang, Y.M. Zhu, Q.B. Zhang, and M.L. Sun, Effect of Rare Earth Cerium on the Microstructure and Corrosion Resistance of Laser Cladded Nickel-Base Alloy Coatings, *J. Mater. Process. Technol.*, 1997, **63**, p 563–567
12. M.A. Arenas, J.J. de Damborenea, A. Medrano, J.A. García, and R. Rodríguez, Corrosion Behaviour of Rare Earth Ion-Implanted Hot-Dip Galvanised Steel, *Surf. Coat. Technol.*, 2002, **158**, p 615–619
13. S.A. Park, S.H. Lee, and J.G. Kim, Effect of Chromium on the Corrosion Behavior of Low Alloy Steel in Sulfuric Acid, *Met. Mater. Int.*, 2012, **18**, p 975–987
14. A.M. Lazar, W.P. Yespica, S. Marcelin, N. Pébère, D. Samélor, C. Tendero, and C. Vahlas, Corrosion Protection of 304L Stainless Steel by Chemical Vapor Deposited Alumina Coatings, *Corros. Sci.*, 2014, **81**, p 125–131
15. S. MajidGhahari, A.J. Davenport, T. Rayment, T. Suter, J.P. Tinnes, C. Padovani, J.A. Hammons, M. Stampanoni, F. Marone, and R. Mokso, In Situ Synchrotron X-ray Micro-Tomography Study of Pitting Corrosion in Stainless Steel, *Corros. Sci.*, 2011, **53**, p 2684–2687
16. H.B. Zhang and Y. Zuo, The Improvement of Corrosion Resistance of Ce Conversion Films on Aluminum Alloy by Phosphate Post-Treatment, *Appl. Surf. Sci.*, 2008, **254**, p 4930–4935
17. S.K. Putatunda, A.V. Singar, R. Tackett, and G. Lawes, Development of a High Strength High Toughness Ausferritic Steel, *Mater. Sci. Eng. A*, 2009, **513–514**, p 329–339

18. J. Yang, D.N. Zou, X.M. Li, and Z.Z. Du, Effect of Rare Earth on Microstructures and Properties of High Speed Steel with High Carbon Content, *J. Iron Steel Res. Int.*, 2007, **14**, p 47–59
19. R.M. Wang, Y.G. Song, and Y.F. Han, Effect of Rare Earth on the Microstructures and Properties of a Low Expansion Superalloy, *J. Alloy. Compd.*, 2000, **311**, p 60–64
20. F.F. Hao, B. Liao, D. Li, T. Dan, X.J. Ren, Q.X. Yang, and L.G. Liu, Effects of Rare Earth Oxide on Hardfacing Metal Microstructure of Medium Carbon Steel and its Refinement Mechanism, *J. Rare Earth.*, 2011, **29**, p 609–613
21. X.L. Li, S.M. He, X.T. Zhou, Y. Zou, Z.J. Li, A.G. Li, and X.H. Yu, Effects of Rare Earth Yttrium on Microstructure and Properties of Ni-16Mo-7Cr-4Fe Nickel-based Superalloy, *Mater. Charact.*, 2014, **95**, p 171–179
22. Y.S. Yin, S. Cheng, S.G. Chen, J.T. Tian, T. Liu, and X.T. Chang, Microbially Influenced Corrosion of 303 Stainless Steel by Marine Bacterium Vibrio Natriegens: (II) Corrosion Mechanism, *Mater. Sci. Eng. C*, 2009, **29**, p 756–760
23. R.G. Duarte, A.S. Castela, R. Neves, L. Freire, and M.F. Montemor, Corrosion Behavior of Stainless Steel Rebars Embedded in Concrete: An Electrochemical Impedance Spectroscopy Study, *Electrochim. Acta*, 2014, **124**, p 218–224
24. Z.X. Yuan, Z.S. Yu, P. Tan, and S.H. Song, Effect of Rare Earths on the Carburization of Steel, *Mater. Sci. Eng. A*, 1999, **267**, p 162–166
25. A.T. Krawczynska, M. Gloc, and K. Lublinska, Intergranular Corrosion Resistance of Nanostructured Austenitic Stainless Steel, *J. Mater. Sci.*, 2013, **48**, p 4517–4523
26. Y.H. Yoo, Y.S. Choi, J.G. Kim, and Y.S. Park, Effects of Ce, La and Ba Addition on the Electrochemical Behavior of Super Duplex Stainless Steels, *Corros. Sci.*, 2010, **52**, p 1123–1129
27. X. Liu, J.C. Yang, L. Yang, and X.Z. Gao, Effect of Ce on Inclusions and Impact Property of 2Cr13 Stainless Steel, *J. Iron Steel Res. Int.*, 2010, **17**, p 59–64
28. Y.J. Kang, J.H. Jang, J.H. Park, and C.H. Lee, Influence of Ti on Non-Metallic Inclusion Formation and Acicular Ferrite Nucleation in High-Strength Low-Alloy Steel Weld Metals, *Met. Mater. Int.*, 2014, **20**, p 119–127
29. J. Alcala, A.C. Barone, and M. Anglada, The Influence of Plastic Hardening on Surface Deformation Modes around Vickers and Spherical Indents, *Acta Mater.*, 2000, **48**, p 3451–3464
30. S.C. Yu, Q.H. Zhu, S.Q. Wu, Y.J. Gong, Y.S. Gong, M.S. Lian, G. Ye, and Y.J. Cheng, Microstructure of Steel 5Cr2lMn9Ni4N Alloyed by Rare Earth, *J. Iron Steel Res. Int.*, 2006, **13**, p 40–44
31. M. Mehdipour, R. Naderi, and B.P. Markhali, Electrochemical Study of Effect of the Concentration of Azole Derivatives on Corrosion Behavior of Stainless Steel in H_2SO_4, *Prog. Org. Coat.*, 2014, **77**, p 1761–1767
32. J.L. Xu, F. Liu, F.P. Wang, D.Z. Yu, and L.C. Zhao, The Corrosion Resistance Behavior of Al_2O_3 Coating Prepared on NiTi Alloy by Micro-Arc Oxidation, *J. Alloy. Compd.*, 2009, **472**, p 276–280
33. T.L. Sudesh, L. Wijesinghe, and D.J. Blackwood, Photocurrent and Capacitance Investigations into the Nature of the Passive Films on Austenitic Stainless Steels, *Corros. Sci.*, 2008, **50**, p 23–34
34. G.H. Wu, C.Y. Wang, Q. Zhang, and P.C. Kang, Characterization of Ce Conversion Coating on Gr-f/6061Al Composite Surface for Corrosion Protection, *J. Alloy. Compd.*, 2008, **461**, p 389–394
35. P.C. Okafor and Y.G. Zheng, Synergistic Inhibition Behaviour of Methylbenzyl Quaternary Imidazoline Derivative and Iodide Ions on Mild Steel in H_2SO_4 Solutions, *Corros. Sci.*, 2009, **51**, p 850–859
36. X.H. Li, S.D. Deng, and H. Fu, Inhibition of the Corrosion of Steel in HCl, H_2SO_4 Solutions by Bamboo Leaf Extract, *Corros. Sci.*, 2012, **62**, p 163–175
37. J.L. Yi and X.M. Zhang, Effects of Ce on Microstructure and Corrosion Resistance of Mg-9Gd-4Y-1Nd-0.6Zr Alloy, *Proc. Eng.*, 2012, **27**, p 815–822
38. Y.T. Ma, Y. Li, and F.H. Wang, Corrosion of Low Carbon Steel in Atmospheric Environments of Different Chloride Content, *Corros. Sci.*, 2009, **51**, p 997–1006
39. Q. Qu, Z.Z. Hao, L. Li, W. Bai, Y.J. Liu, and Z.T. Ding, Synthesis and Evaluation of Tris-Hydroxymethyl-(2-Hydroxybenzylidenamino)-Methane as a Corrosion Inhibitor for Cold Rolled Steel in Hydrochloric Acid, *Corros. Sci.*, 2009, **51**, p 569–574
40. E. Stoyanova, D. Nikolova, D. Stoychev, P. Stefanov, and T. Marinova, Effect of Al and Ce Oxide Layers Electrodeposited on OC4004 Stainless Steel on its Corrosion Characteristics in Acid Media, *Corros. Sci.*, 2006, **48**, p 4037–4052